# Lawrence Berkeley Laboratory

UNIVERSITY OF CALIFORNIA

## Materials & Chemical Sciences Division

# The Mechanical Properties of Drawn Dual Phase Steel Wire

S.M. Miyasato
(M.S. Thesis)

December 1987

DO NOT MICROFILM
COVER

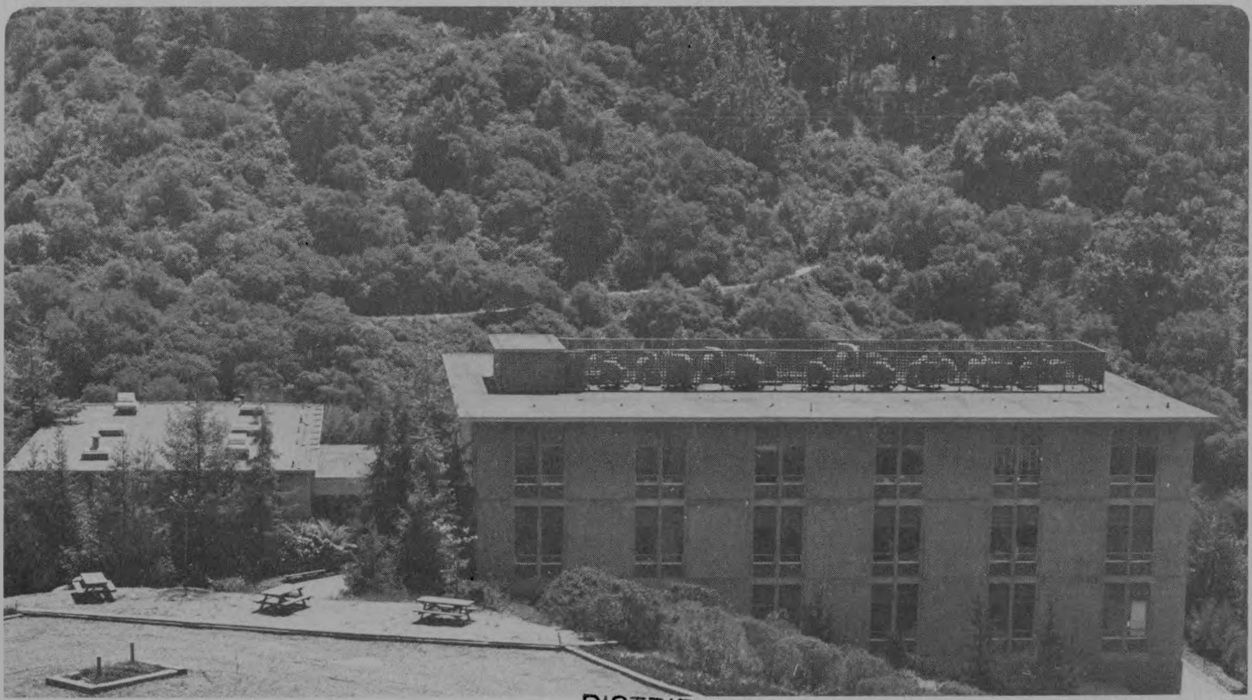

Prepared for the U.S. Department of Energy under Contract Number DE-AC03-76SF00098.

---

LBL--29060
DE90 013870

# The Mechanical Properties of Drawn Dual Phase Steel Wire

Shelly Midori Miyasato
M. S. Thesis

Department of Materials Science and Mineral Engineering
University of California at Berkeley

and

Materials and Chemical Sciences Division
Lawrence Berkeley Laboratory
1 Cyclotron Road
Berkeley, CA 94720

December 1987

This work was supported by the Director, Office of Energy Research, Office of Basic Energy Sciences, Chemical Sciences Division, of the U.S. Department of Energy under Contract No. DE-AC03-76SF00098.

# TABLE OF CONTENTS

# THE MECHANICAL PROPERTIES OF DRAWN DUAL-PHASE STEEL WIRES

Shelly Midori Miyasato

Master of Science Thesis
Department of Materials Science and Mineral Engineering
University of California at Berkeley
Berkeley, CA 94720
December 1987

## ABSTRACT

Dual-phase steels are a class of composite high strength, low alloy steels. The outstanding properties of ferrite/martensite dual-phase steels include its very high work-hardening rates and resistance to fatigue failure. The high work-hardening rates make dual-phase steels ideal for large strain cold forming applications, since high strengths may be achieved with less deformation. Dual-phase steels have been shown to be especially suited to wire drawing. In this study, Fe/xC/2Si alloys were heat treated to obtain different ferrite/martensite morphologies and relative volume fractions, then the work-hardening rates at true plastic strain $\varepsilon=0.006$ were determined. Wires were then drawn from 4.2 to 1.4 mm in diameter, which corresponded to a strain of $\varepsilon=2.2$, and tested in tension and fatigue. The early work-hardening rate increased with increased volume fraction of martensite, increased strength of martensite, and decreased ferrite/martensite interface coherency. The wire drawing limit was raised by discouraging void formation at ferrite/martensite interfaces and shear cracking through martensite particles. The lowest void density was obtained in a structure of fibrous martensite with coherent ferrite/martensite interfaces (i.e. produced by intermediate quenching). The fatigue limit of drawn dual-phase wires was ~600 MPa, or 25-30% of the ultimate tensile strength, which appears to be higher than that of similar pearlitic steel wire. There was no superior microstructure for fatigue resistance in wires, as any morphology differences which exist in the initial structure are indistinguishable after heavy deformation. Fatigue cracks initiated on the wire surface at inclusions, sites of interface decohesion and martensite particle cracking, and in the interior of the wire at large cracks which formed during wire drawing. Attempts at monitoring small crack growth by replication were unsuccessful.

# 1. INTRODUCTION

## 1.1. General background of dual-phase steel wire

### 1.1.1. Dual-phase steels

Duplex ferrite-martensite, or dual-phase, steel is a class of low carbon, low alloy steels [1,2] with a composite microstructure of strong martensite (M) in a ductile ferrite ($\alpha$) matrix. The significant properties of dual-phase steels include continuous yielding, high initial work-hardening rate, good formability and high tensile strength, and the combination of these properties have made dual-phase steels attractive for many structural applications. Five conferences have been dedicated to exploring the relationship between microstructural elements (e.g. volume fraction of martensite, morphology and composition) and mechanical properties (e.g. tensile strength, Charpy impact toughness and fatigue resistance) of as heat-treated dual-phase steels [**3-7**].

Dual-phase steel microstructures are produced by various thermal and thermo-mechanical treatments, which yield different ferrite/martensite morphologies depending on the structure prior to heat-treatment in the intercritical ($\alpha$+$\gamma$) field. Three are of interest in this investigation. The intermediate quenching (IQ) process involves heating a martensitic structure into the ferrite/austenite ($\alpha$+$\gamma$) two-phase field, then quenching. The result is packets of parallel fibers of martensite in continuous ferrite [**2,8**]. The intercritical annealing (IA) process involves heating an initially pearlitic structure into the intercritical field, then quenching. This yields globular martensite grains on ferrite grain boundaries [**9-10**]. The controlled rolling (CR) treatment involves austenitizing, rolling above the austenite recrystallization temperature, rolling below the austenite recrystallization temperature, rolling in the intercritical field, then quenching [**11-12**]. The resulting microstructure is elongated martensite surrounded by small, equiaxed ferrite grains. The heat-treatments and resulting microstructures are shown in Figure 1.

During heating in the ($\alpha$+$\gamma$) region, the carbon partitions mostly into the austenite phase. The yield strength of martensite, $\sigma_Y$ is proportional to the square root of the carbon content,

$$\sigma_Y \sim k \sqrt{C}$$

where k is a constant, The amount of carbon in the martensite phase ($C_M$) is determined by the lever rule in the ($\alpha+\gamma$) region of the phase diagram. Thus, for an alloy with carbon content $C_o$, the strength of martensite phase may be increased by decreasing the martensite volume fraction.

The amount of carbon in the martensite phase ($C_M$) should be kept below ~0.4 wt.%, however. Above $C_M \approx 0.4$ wt.% twinned plate martensite forms. The lattice shear required by the austenite to martensite transformation occurs by twinning, resulting in a brittle martensite structure unsuitable for heavy deformation applications. At low carbon contents, dislocated lath martensite forms. This martensite is relatively deformable, and its presence is desirable.

### 1.1.2 Dual-phase steel wires

The deformation properties of dual-phase steel make it suitable for large strain, cold forming applications, such as wire drawing [**13-14**]. The research program at Berkeley has developed dual-phase wires continuously drawn to tire cord size with strengths exceeding 400 ksi (2700 MPa) that require no costly intermediate patenting treatments during production [**15-16**]. However, most wire applications involve cyclic loading, and the fatigue behavior of wires is still not well understood. There is very little information on the fatigue resistance of heavily deformed material in general [**17**]. Thus, the purpose of this study was to analyze the fatigue behavior of continuously drawn dual-phase wire.

## 1.2. Fatigue resistance of dual-phase steels

### 1.2.1 Closure contribution

Dual-phase steels display excellent fatigue resistance in the pre-drawn state [**18-20**]. The primary reason the dual-phase structure resists crack propagation is the composite microstructure which promotes crack tip shielding. The tortuous crack path results in an extremely high fatigue threshold stress intensity ($\Delta K_o$), for example, $\Delta K_o = 20.1\ \mathrm{MPa}\sqrt{m}$ in AISI 1008 [**20**]. Minakawa and McEvily [**21**] noted that $\Delta K_o$ values increased with increasingly tortuous crack path, and postulated that high $\Delta K_o$ values result from roughness-induced crack closure. This has been verified by Suresh and Ritchie [**22**] and Wasynczuk et al. [**23**], who found that $\Delta K_o$ increased as grain size increased (increased tortuousity), and as load ratio decreased (increased crack closure). The morphology for highest fatigue crack resistance is a large grained, globular martensite structure [22], which also has the lowest drawability [15].

### 1.2.2. Effect of changes in martensite properties

The fatigue behavior is strongly related to the martensite volume fraction, distribution, shape and strength. Suzuki and McEvily [18] found that continuous martensite constrained plastic deformation at the crack tip, and so increased the threshold. The effect of martensite distribution and shape was investigated by Tomota [24], who found that under fully reversed cyclic loading, the Bauschinger effect was greater in intercritically annealed (IA) samples than in intermediately quenched (IQ) samples. The thresholds of intermediately quenched (IQ) and intercritically annealed (IA) samples were compared at constant volume fraction of martensite (55%), and it was found that the threshold of intercritically annealed (IA) samples was 25% higher than that of intermediately quenched (IQ) structure [25].

### 1.2.3. Fatigue crack initiation

The initiation site of fatigue cracks have been examined for different volume fractions of martensite. Cracks initiated at ferrite/martensite grain boundaries in samples with 19% martensite, but initiated at slip bands adjacent to the ferrite/martensite interface in the ferrite when the martensite volume fraction was increased to 50% [26]. By changing the martensite volume fraction, the character of the martensite (twinned or dislocated lath) may also have been changed; this effect was not discussed. Initiation at ferrite/martensite interfaces was also observed by Wan et al. [27] at 25% martensite, who found that cracks grew primarily along ferrite/martensite grain boundaries but grew through martensite particles during later stages of crack propagation in intermediately quenched (IQ) samples.

## 1.3. Fatigue behavior of dual-phase wire

### 1.3.1. Fatigue of wire

Most applications of dual-phase wire involve cyclic loading so it is important to understand the response to fatigue in order to design for crack resistance. Little research has been devoted to examining the fatigue behavior of wire. The fatigue behavior of pearlitic wires has been recently studied in depth by Verpoest [28], who found that the initiation of fatigue cracks could be attributed to three types of surface defects:

1. cracks in the thin martensite layer, which formed if the wire was heated during drawing because of poor lubrication;
2. longitudinal grooves formed during drawing which coalesce into a single defect of sufficient size so as to present a crack initiation site; and
3. inclusions or holes left by inclusions.

Crack propagation in pearlitic wire was studied as a function of drawing strain. Although the fatigue limit increased as strain increased, the ratio of the fatigue limit to ultimate tensile stress decreased . The fatigue threshold was also found to decrease as strain increased. For a drawing strain of $\varepsilon=2.36$, the fatigue limit as calculated for fully reversed loading ($R= K_{min}/K_{max}=-1$) was 500 MPa (73 ksi), the ratio of fatigue limit to tensile strength was 0.24, and the threshold was $\Delta K_o = 3.53$ MPa$\sqrt{m}$. Electrolytic polishing was found to increase the fatigue limit by reducing surface defect depth, which nearly eliminated initiation at broken martensite and longitudinal grooves.

### 1.3.2. Fatigue of dual-phase wire

Fatigue of dual-phase wire has been studied as a function of martensite volume fraction in intercritically annealed (IA) samples [25]. The threshold decreased monotonically with increased martensite content, from ~2.9 MPa$\sqrt{m}$ at 27% martensite volume fraction to 1.8 MPa$\sqrt{m}$ at 80% martensite. This behavior is the reverse of the threshold behavior of pre-drawn dual-phase material . The effect of the morphology of the pre-drawn structure on the fatigue behavior of wires still remains to be examined.

### 1.3.3. Relation to work-hardening rate

Drawn wires, because of their stored cold-work, undergo considerable softening due to dynamic recovery during cyclic loading [29-30]. Thus, drawn strength should be maximized so that the strength level after softening has occurred is still acceptable. Drawn strength is related to the deformation behavior during drawing, which in turn is determined by the work-hardening rate of the starting structure. Therefore, the work-hardening rate of the starting material has an effect on the fatigue behavior of wires.

## 1.4. Work-hardening rate

The work-hardening rate of dual-phase steels is known to be extraordinary. The work-hardening rate of three vanadium containing dual-phase steels was found to be nearly 7000 MPa (1000 ksi) at 0.02 true strain, twice the work-hardening rate of SAE 950X [**31**]. The high initial work-hardening rate of dual-phase steel is the result of the high density of mobile dislocations present in the early stages of deformation. Dislocations are introduced during heat treatment, as the austenite to martensite transformation produces a large number of dislocations in the ferrite to accommodate the martensitic lattice shear. These dislocations are unpinned and so can move at very small strains, which suppresses the yield-point phenomenon. The ferrite phase must be free of solute atoms, which would pin the initial dislocations and raise the yield strength. The tensile deformation of dual-phase steels is commonly divided into three stages [**32-34**]:

Stage I, from $\varepsilon \approx 0.001$ to $\varepsilon \approx 0.01$, involves the yielding of the ferrite phase only, so the flow stress is related to the mean free path for dislocation motion in the ferrite phase. The compressive stress in the martensite from the constraint of the surrounding ferrite matrix is also relieved during this stage.

Stage II, from $\varepsilon \approx 0.01$ to $\varepsilon \approx 0.05$, is characterized by smaller decreases in work-hardening rate with increased strain. The martensite grains, which still deform elastically in tension, constrain the deformation of neighboring ferrite, which increases work-hardening. In steels with "grains" of retained austenite, another contribution to the work-hardening in this stage is made by the transformation of retained austenite to martensite. Cribb and Rigsbee [**34**] noted that the retained austenite in uniaxial tensile specimens tripped into martensite before the strain at which necking occurred. The dislocations generated by this transformation would add to the dislocations due to multiplication.

Stage III occurs because of dynamic recovery at high strains, just prior to the onset of macroscopic non-uniform deformation (necking), and is identified by more rapid decreases in rate of work-hardening with strain. The existing dislocations begin to form cells, and higher stresses are required to generate additional dislocations required for deformation. The work-hardening rate during stage III is independent of second phase volume fraction because at these high stresses, martensite deforms as well [**34**].

## 1.5. Investigated variables

### 1.5.1. Work-hardening rate study

The initial work-hardening rate was examined as a function of martensite volume fraction, morphology and strength. The martensite volume fraction was varied from 20-50%, for each martensite morphology. The morphologies used in this investigation were the packets of parallel fibers of martensite embedded in continuous ferrite produced by intermediate quenching (IQ), fine globular martensite at ferrite grain boundaries produced by intercritical annealing (IA), and fibrous martensite surrounded by equiaxed ferrite grains produced by controlled rolling (CR). The effect of tempering a vanadium containing alloy was also be studied. The strength of the martensite varied inversely with volume fraction for the same alloy by the lever rule. To study the effect of martensite strength at a constant volume fraction, several alloys differing only in carbon content were used. The strength of the wire for fatigue applications was optimized.

### 1.5.2. Fatigue of wires study

The effect of morphology on the endurance limit of drawn dual-phase steels was investigated using the fibrous martensite (IQ) and globular martensite (IA) initial structures with 20% martensite. The volume fraction was chosen to be low, since it is known that a 20% martensite volume fraction delays the drawing limit [35]. The fatigue crack initiation sites were determined on unpolished samples, and differences in crack path between the two samples were determined.

### 1.5.3. Silicon alloys

Silicon alloys are used primarily because silicon raises the $A_3$ temperature, which increases the area of the $(\alpha+\gamma)$ region of the phase diagram and thereby ensures that temperature fluctuations during heat treatment have a small effect on martensite volume fraction. Silicon also provides solid-solution strengthening of ferrite, which reduces the deformation necessary to achieve a certain strength. A complete discussion on the effect of silicon additions is contained in a paper by Koo and Thomas [36].

## 2. EXPERIMENTAL PROCEDURES

### 2.1. Alloy preparation

The alloy chemical compositions are listed in Table 1. Three alloys, all containing ~2 wt.% silicon, but different carbon contents were, provided by Nippon Kokan K.K., Japan. They were vacuum induction melted, cast in 50 kg ingots, homogenized at 1250°C for 3 hours, and rolled into plates 0.75 in (20 mm) thick. Square bars were cut from the plates and hot open die forged to 0.25 in (7 mm) diameter rods.

The vanadium containing alloy was provided by Sandia National Laboratories, Albuquerque, N.M. It was vacuum induction melted in 130 kg ingots, vacuum arc remelted, homogenized at 1100°C for 16 hours, and rolled into plates 0.5 in (13 mm) thick. Square bars were cut from the plates and hot forged to 0.25 in (7 mm) diameter rods.

### 2.2. Heat treatment

Specimens 5 in (120 mm) long were cut from the rods for heat treatment. Three different heat treatments were used to generate different ferrite/martensite morphologies according to the schemes presented in Figure 1.

Samples with varied martensite volume fractions were produced from the three silicon alloys with different carbon contents. Additionally, the vanadium alloy was treated by intermediate quenching (IQ). Material treated by intermediate quenching was austenitized for 30 minutes and quenched in agitated ice brine to form 100% martensite. Then it was annealed in the two-phase ($\alpha+\gamma$) field for 10 minutes and again quenched in agitated ice brine. The annealing temperature was chosen to produce the desired martensite volume fraction. Heating was conducted in a vertical tube furnace under flowing argon atmosphere.

The silicon alloy with 0.1%C was also treated by intercritical annealing (IA). It was austenitized for 30 minutes and air-cooled to form ferrite/pearlite, then annealed in the two-phase field for 10 minutes and quenched in agitated ice brine. The intercritical temperature was chosen to match the 30% martensite volume fraction obtained during intermediate quenching. Heating was again conducted in a vertical tube furnace under flowing argon atmosphere.

The vanadium alloy was treated by controlled rolling (CR). The area was reduced by 50% during rolling at 1100°C (just above the austenite recrystallization temperature), then by 30% at 1020°C (below the recrystallization temperature), and finally by 35% at 950°C (in the two-phase field). After the final pass, the rod was quenched in agitated ice brine. Rolling was done on a two-high reversing bar mill in the laboratory. Temperatures were monitored with a thermocouple inserted at the center of the circular cross-section 1.5 inch (5 mm) from the back end of the rod. To prevent fracture of the thermocouple wires at the end of the rod, the thermocouple was packed in with alumina powder for lubrication, and the back end of the rod was gradually reduced in diameter to form a truncated cone.

The intercritical temperatures used to achieve the required volume fractions of martensite are listed in Table 2. Tempering of intermediately quenched and controlled rolled samples was done in a salt bath at 200°C for 1 hr.

### 2.3. Wire drawing

The heat-treated rods were machined to reduce the diameter from 0.25 in (6.4 mm) to 0.17 in (4.2 mm) to lower the load on the laboratory wire drawing machine. After machining, the rods were ground and cleaned. An eight-pass drawing schedule (see Table 3) was used to achieve 89% total reduction in area. This gave a final wire diameter (~1.4 mm) convenient for the fatigue testing capabilities in the laboratory. The reduction in area per pass monotonically decreased from 34% to 18%. No intermediate tempers or anneals were used. Rods were swaged at one end, then drawn through 6°-8° semi-die angle conical carbide and diamond dies. Both the rod and dies were brushed with Dupont Vydax freon-teflon dispersion lubricant. The drawing speed was 30 mm/sec for all passes. Front-end material which had been swaged was not used in the investigation because of the different deformation history.

### 2.4. Mechanical testing

#### 2.4.1. Tensile testing

Subsize cylindrical tensile test specimens were prepared from as-heat-treated material according to specifications in Figure 2. The center of the gage section was further ground into an hourglass shape (reduction in area of 5-10%) to ensure failure in the center of the gage section. The smallest diameter was measured on a travelling microscope with a vernier scale with 10 μm resolution. The gage length was manually scribed onto the specimen and measured on the travelling microscope. After failure the gage diameter and lengths were measured on the travelling microscope. These measurements were used to calculate the reduction in area (RA) and total elongation ($\varepsilon_t$ ). Other tensile properties, including 0.2% yield strength, were determined from recorded load-displacement strip charts.

Drawn wires were tested in specially designed grips which required no reduction in area in the gage section. The grips featured leafsprings that applied successively lower loads along the length of the wire in the grips to reduce the stress discontinuity at the mouth of the grip (see Figure 3). Gage lengths of drawn wires were 2 in (5 mm) long. All tensile properties were determined from load-displacement data.

Tensile tests were performed on a 25 kN servo-hydraulic Instron testing machine at a crosshead speed of 0.02 in/min (0.5 mm/min) in laboratory air.

### 2.4.2. Fatigue testing

Wires from 0.1/IQ/30 and 0.1/IA/30 of diameter 0.55 in (1.4 mm) and length 6 in (300 mm) were tested in the as-drawn condition: no polishing or stress-relieving was done on the gage section. A 5 kN servo-hydraulic Instron testing machine was operated under load control, with sinusoidal frequency varying from 20 to 55 Hz. The tests were conducted at a load ratio of R=0.05 in laboratory air at ambient temperatures. The leafspring grips were also used for fatigue testing. To further reduce the probability of failure at the mouth of the grips, the lengths of the wire sample which would be held in the grips were sand blasted to put the surface in compression.

Wires for small crack data were manually ground and polished, with final polishing by 6 μm diamond polish in the longitudinal direction. Small cracks were replicated with strips of cellulose-acetate 0.005 in (0.13 mm) thick that were softened in acetone. The strips were pressed against the wire with brass molds to replicate half the surface area of the wire test section. The strips were applied four times at each test interruption, rotating the mold 90° each time so that the entire surface was adequately recorded. The replica was held by hand until it dried, and then it was removed. The replica was affixed and flattened onto a glass slide coated with double-sided tape.

## 2.5. Microscopy

### 2.5.1. Light optical microscopy

Samples of heat-treated rods and drawn wires for microstructural examination were cut with a flood cooled cut-off wheel, then mounted in Bakelite in both transverse and longitudinal sections. The mounts were wet ground by hand on 180 through 600 grit SiC papers, then automatically polished with 6 and 1 micron diamond paste lubricated with polishing oil. Fatigue fractures for crack path analysis were mounted longitudinally in conductive Bakelite and prepared similarly to the untested wires, taking care that the diametrical cross-section was revealed after grinding. Polished samples were etched with 5% nital and observed under a Zeiss Ultraphot II metallograph.

Examination of cellulose-acetate replicas was facilitated by using the Nomarski interference technique and by lightly gold coating the replicas.

### 2.5.2. Scanning electron microscopy and metallography

Samples for microstructural examination under a scanning electron microscope (SEM) were prepared as for light optical microscopy, then gold-coated (~50 nm thickness). Tensile and fatigue fracture surfaces were secured in aluminum foil and observed uncoated. A JEOL JSM-35 equipped with a $LaB_6$ filament was operated at 25 kV. The lighter-contrast phase is martensite and the darker-contrast phase is ferrite in all SEM micrographs.

The volume fraction of martensite was determined by line intercept method on both light microscope and SEM micrographs. The magnification chosen in each case was dependent on the martensite size.

Void density measurements were made on scanning electron microscope images at 2000X magnification. The voids were counted across the diameter in two separate areas to ensure representative measurements. The SEM was used to ease differentiation between void types.

### 2.5.3. Transmission electron microscopy

A low speed Isomet saw with a diamond wafering blade was used to cut slices, 0.025 in (600 µm) thick, from heat-treated rods. Both longitudinal and transverse slices were taken from the control-rolled rod since texture was introduced during rolling. The slices were ground to 0.005 in (130 μm) thick on wet SiC papers. Then 0.12 in (3 mm) diameter disks were punched from the slices. The disks were further reduced in thickness to 0.002 in (50 μm) by grinding on 600 grit wet SiC papers. Foils were prepared by electropolishing to perforation with a Struers Electropol in an electrolyte of 70% ethanol, 25% glycerol and 5% perchloric acid cooled to $T = -15°C$ with a constant applied voltage of 11V. Foils were examined with a Philips EM 301 transmission electron microscope (TEM) operated at 100 kV.

# 3. RESULTS

## 3.1. Pre-drawn properties

### 3.1.1. Initial microstructures

Typical dual-phase microstructures produced by intermediate quenching (IQ), intercritical annealing (IA) and controlled rolling (CR) are shown in Figure 4. The intermediately quenched structure consisted of elongated martensite grains lying parallel to a prior austenite grain variant in continuous ferrite. The intercritically annealed structure was composed of globular martensite grains on ferrite grain boundaries. Controlled rolling produced martensite particles which are elongated in the drawing direction and surrounded by equiaxed ferrite grains. No effect of tempering could be discerned by scanning electron microscopy. The volume fractions of martensite obtained in each sample are included in Table 2.

Transmission electron microscopy was performed to determine the nature of the martensite phase, using established techniques [37]. Twinned martensite was identified in 0.2/IQ/30 (Figure 5). Figure 6 shows a bright field/dark field pair of TEM micrographs of twinned plate martensite in 0.2/IQ/30, as well as a diffraction pattern showing the two martensite patterns. The martensite in 0.1/IQ/30 (Figure 7), 0.1/IA/30 (Figure 8) and 0.1/CR/20 was all dislocated lath-type, which has thin interlath retained austenite that is heavily deformed so that the selected area diffraction pattern shows $<111>_M // <110>_\gamma // <100>_M$. The bright field/dark field contrast shown in Figure 9 was representative of all the laths observed. Tempering the vanadium-containing alloy caused the precipitation of fine vanadium carbides, as shown in Figure 10.

### 3.1.2. Tensile test results

The load-displacement curves displayed typical dual-phase steel characteristics such as little elastic deformation, low yield strength and continuous yielding. The tensile properties of the different structures are included in Table 4. The highest tensile strength was achieved by 0.2/IQ/30, which also had the lowest total elongation and reduction in area. Tempering of 0.1/V/IQ/20 and 0.1/V/CR/20 caused the reappearance of the discontinuous yield point and simultaneously increased ductility and decreased strength. A comparison of the engineering stress-strain curves for the control-rolled samples before and after tempering is shown in Figure 11. Figure 12 shows the increased post-uniform deformation (necking) after tempering. Higher magnification fractography shows that the dimple size is about the same in both cases.

### 3.1.3. Work-hardening rate

The work-hardening rates at the true plastic strain of $\varepsilon=0.006$ are listed in Table 5. The globular martensite morphology had a higher initial work hardening rate than the fibrous martensite. The higher the overall carbon content of the alloy, the higher the work-hardening rate, holding volume fraction and martensite morphology constant. Also, larger volume fractions of martensite raised the work-hardening rate, holding overall carbon content and martensite morphology constant. Tempering decreased the initial work hardening rate by 21% for 0.1/V/IQ/30 and by 63% for 0.1/V/CR/20.

## 3.2. Wire production, structure-property relations

### 3.2.1. Structure and drawability

Three heat-treated rods, 0.2/IQ/30, 0.1/IQ/30 and 0.1/IA/30, were each drawn to total strain of $\varepsilon=2.22$. The drawing limit, which was defined as the diameter beyond which breakage occurred at every subsequent pass, was reached at drawing strain of $\varepsilon=1.30$, while the drawing limit for 0.1/IQ/30 and 0.1/IA/30 was not reached after a drawing strain of $\varepsilon=2.22$. The longitudinal cross-sections of the drawn structures drawn to $\varepsilon=2.22$ are shown in Figure 13. The structure of 0.1/IQ/30 deformed smoothly in comparison with 0.2/IQ/30 and 0.1/IA/30, both of which contained non-deformable martensite particles.

Observation of the drawn structure at the final diameter also revealed a large number of voids, and typical examples are shown in Figure 14. Voids were seen about inclusions

(Figure 14a), at ferrite/martensite interfaces both normal and parallel to the loading direction (Figures 14b and 14c), and through martensite particles (Figure 14d). Various stages of martensite particle cracking were observed, and the shearing and crack initiation of martensite are shown in Figure 15. The void densities of the drawn microstructures are listed in Table 6. The higher carbon 0.2/IQ/30 had the highest density of voids, 88% higher than 0.1/IQ/30. The large increase is primarily attributed to the higher incidence of decohesion at the end of martensite grains, or normal decohesion. The shape of the pre-drawn martensite had less of an effect on void density: the 0.1/IA/30 structure had a 58% higher void density than 0.1/IQ/30.

### 3.2.2. Tensile properties of drawn wires

The tensile properties of the drawn wires are included in Table 7. Although 0.2/IQ/30 achieved the highest strength, it also had the lowest ductility, as in the pre-drawn state. The fractured surfaces in Figure 16 show that 0.2/IQ/30 underwent a much smaller amount of necking than 0.1/IQ/30 or 0.1/IA/30. The lower carbon alloys had typical ductile fracture surfaces: a high magnification image of the 0.2/IQ/30 fracture surface, however, revealed broken martensite particles (indicated by "M") at the bottoms of large dimples. Low magnification fractographs reveal considerable secondary cracking in both 0.1/IQ/30 and 0.1/IA/30, and none in 0.2/IQ/30.

## 3.3. Fatigue of wires

### 3.3.1. S-N curves

The drawn wires were tested in tension-tension fatigue. One-half of all specimens fractured at the mouth of the grips, even with the action of the leafsprings. Sandblasting the lengths in the grip did not increase the probability of failure in the gage length. Only the specimens which failed in the gage length were plotted on S/N diagrams and examined to determine fatigue crack initiation and growth behavior. S/N plots were obtained for 0.1/IQ/30 and 0.1/IA/30 and are presented in Figure 17. The fatigue limits (defined as the highest stress amplitude at which the wire does not fail in $10^6$ cycles) are at alternating stresses of about 35% of the ultimate tensile strength, as calculated for fully reversed loading (R=-1) using the modified Goodman equation. There was a very large statistical scatter in the data which prevents any quantitative comparison of the two curves, although the fatigue limit of 0.1/IA/30 appears to be slightly higher than 0.1/IQ/30.

### 3.3.2. Fractography of fatigue drawn samples

Fractography revealed that three possible initiation sites for the fatigue cracks are at surface inclusions, surface decohesion of ferrite and martensite, and less frequently at large internal cracks formed during drawing. Examples of these initiators are shown in Figure 18.

The fatigue fracture surfaces of 0.1/IQ/30 and 0.1/IA/30 are compared in Figure 19 where the fatigue initiation sites are indicated by arrows. They were tested at a ratio of alternating stress to ultimate tensile stress of ~35% (as calculated for fully reversed loading, R=-1, by the Goodman relation). The fatigue crack growth zones in both 0.1/IQ/30 and 0.1/IA/30 are visibly penny-shaped. Large amounts of secondary cracking are seen in the fast fracture zone, similar to that in the tensile overload failures.

The early, middle, and final stages of fatigue crack growth, as well as the fast fracture region are recorded in Figures 20 and 21. The fatigue cracks grew smoothly in the early stage, and became progressively less smooth as the crack propagated. Overall, the fatigue cracks propagated normal to the direction of cyclic loading, as shown in Figure 22, which compares the typical fatigue regions as observed in longitudinal cross-section for 0.1/IQ/30 and 0.1/IA/30. The higher magnification micrographs of fatigue crack propagation in Figures 23 and 24 show that the crack did not significantly deflect at ferrite/martensite interfaces. No significant differences in fatigue crack path tortuosity between 0.1/IQ/30 and 0.1/IA/30 is visible by either macroscopic or microscopic observation.

### 3.3.3. Drawn structure after cyclic loading

The cyclic loading changed the ferrite/martensite interface, as shown in Figure 25. The interface displays steps in both 0.1/IQ/30 and 0.1/IA/30 which were not present before fatigue. The roughening appears more severe for 0.1/IQ/30 than 0.1/IA/30.

# 4. DISCUSSION

## 4.1. Work-hardening rate

### 4.1.1. Relative effects of martensite volume fraction and morphology

The early work-hardening rate was found to depend on the carbon content in the martensite phase at constant martensite volume fraction and morphology. The specimen 0.2/IQ/30 ($C_M$=0.64 wt.%) had an initial work-hardening rate of 17,200 MPa while that of 0.1/IQ/30 ($C_M$=0.33 wt.%) was 13,700 MPa. Thus a reduction in martensite phase carbon content ($C_M$) of 50% resulted in a decrease in work-hardening rate of ~20%. Similarly, when 0.1/IQ/30 and 0.05/IQ/30 are compared, a reduction in $C_M$ of 50% resulted in a decrease in work-hardening rate of ~15%. The effect on work-hardening rate of carbon content is explained by recalling that as the carbon content of the martensite phase ($C_M$) increases, the volume expansion required by the austenite to martensite transformation increases and hence the initial dislocation density increases. These transformation-induced dislocations are able to interact at very low strains. Therefore, the early work-hardening rate increases as carbon content in the martensite increases.

The effect of martensite volume fraction on the early work-hardening rate is evaluated by comparing the work-hardening rate of 0.2/IQ/20 and 0.2/IQ/30. A 40% increase in work-hardening rate resulted from a 50% increase in martensite volume fraction. Because the martensite volume fraction was changed using the same alloy, the martensite carbon content, $C_M$ also changed. The decrease in $C_M$ of 30% should have corresponded to a decrease in work-hardening rate, so the effect of martensite volume fraction of martensite overrides the effect of martensite carbon content. This is true to a smaller degree for 0.05/IQ: a 30% increase in martensite volume fraction and a 30% decrease in martensite carbon content caused a 10% increase in the early work-hardening rate.

The work-hardening rate of 0.1/IA/30 was 30% higher than that of 0.1/IQ/30. A possible strengthening mechanism is the reduction of dislocation slip length in the ferrite matrix. The slip length in 0.1/IA/30 is the average ferrite grain size as the coarse,globular martensite grains which decorate ferrite grain boundaries. The slip length in 0.1/IQ/30 is more complicated. A first-approximation of the slip length in ferrite involved identifying the possible slip directions, the orientation of these slip directions with respect to the martensite fiber orientation, and the percentage of generated dislocations which would glide in the slip directions assuming an arbitrary loading direction with respect to the martensite fiber orientation. This estimate ignored the constraint of neighboring grains on the deformation of the model ferrite/martensite packet. The slip systems in b.c.c. ferrite are {110} <111>, and the elongated martensite particles have <110> directions aligned with <110> ferrite directions in a given packet. Estimates of the slip lengths in 0.1/IA/30 and 0.1/IQ/30 are 7.6 μm and 7.0 μm respectively, which indicate that 0.1/IQ/30 should have a higher work-hardening rate than 0.1/IA/30, which disagrees with experimental results. The effect of the assumptions in the above approximation of slip length may account for the discrepancy. For example, if more dislocations in 0.1/IQ/30 glide parallel to the martensite fibers, the slip length will increase. Also, the assumed simple distribution of martensite fibers in 0.1/IQ/30 underestimated the slip length. The incoherent ferrite/martensite interfaces in 0.1/IA/30 could affect the slip length: an "effective" slip length could be defined to be less than the actual martensite particle spacing. The incoherent interfaces encourage dislocation cross-slip and so tangles, which would account for the higher early work-hardening rate.

### 4.1.2. Effect of tempering

Tempering produced fine vanadium carbides (or carbonitrides) in the ferrite phase [43]. The carbide plates, which were ~50 nm in diameter, showed dislocation loop contrast characteristic of coherent precipitates. The precipitate-free zone that is seen in Figure 10 is particularly susceptible to failure. Vanadium carbides form at such low temperatures because of the dislocations present in the ferrite from the martensitic transformation [44]. Precipitation in ferrite has also been studied in niobium containing dual-phase steels [45]. The formation of hexagonal ε-carbide was discouraged by the silicon content of the alloy [43]. The tempering lowers the initial work-hardening rate by lowering the dislocation density in the ferrite. During tempering, some carbon atoms migrate to dislocations, effectively pinning them and causing the increase in yield strength and the reappearance of a defined yield point. This was also seen by Speich et al. [46] on the tempering of Mn and Mn-Si-V dual-phase steels. Tempering also relieved the stress in the martensite caused by the lattice shear.

## 4.2. Drawn wire structure, void formation and drawing limit

The drawn structures for three specimens, 0.2/IQ/30, 0.1/IQ/30 and 0.1/IA/30 are presented in Figure 12. The structures vary in void density, which is quantified in Table 6, and this is expected to affect the drawability of the wires.

The voids in the 0.2/IQ/30 structure are primarily caused by decohesion at the ends of the martensite particles and by shear cracking of martensite. The martensite particles are not as deformable as the particles in 0.1/IQ/30, and this difference is attributed to the different character of the martensite. As shown in Figure 6, the martensite in 0.2/IQ/30 is twinned which is lower in ductility although higher in strength due to the higher carbon content. The martensite in 0.1/IQ/30 is dislocated lath type, which is more deformable than twinned martensite, but is still less deformable than the surrounding ferrite. Both types of martensite are coherent with the ferrite matrix in the pre-drawn condition. However, the compatibility of the ferrite/martensite interfaces after a large amount of deformation depends on the nature of the martensite present. The presence of dislocated lath martensite in 0.1/IQ/30 lowered the void density by a factor of 8 when compared to that of 0.2/IQ/30, excluding the voids due to inclusions. The smaller density of voids due to decohesion at the ends of martensite particles and shear cracking of martensite in 0.1/IQ/30 is due to the prolonged interfacial coherency. Hence, high numbers of dislocations are not required at ferrite/martensite interfaces and void formation is postponed.

The effect of the initial martensite morphology on the void density in drawn wires is seen by comparing the void densities of 0.1/IQ/30 and 0.1/IA/30. The fibrous martensite of 0.1/IQ/30 have many long, parallel, coherent interfaces with surrounding ferrite which can carry a high load, while the shorter, incoherent ferrite/equiaxed martensite interfaces of 0.1/IA/30 are not as efficient at load transfer and are susceptible to void formation. This explains the observed higher density of voids caused by decohesion in 0.1/IA/30 than in 0.1/IQ/30. The dependence of void density on the martensite morphology has been reported by Sidjanin et al. [47]. Note that the parallel <110> directions in ferrite as well as martensite produced by intermediate quenching is ideal for wire-drawing, which induces a <110> texture in b.c.c materials.

The void density, then, is affected by the initial microstructure and itself affects the drawability of wires. Wires of 0.2/IQ/30 were drawn to $\varepsilon=1.30$ without breakage (i.e. the drawing limit), while the lower carbon wires could be drawn to $\varepsilon=2.22$ without breakage.

The drawing limit was not determined for the lower carbon wires; however, Ahn has reported that 0.1/IA/20 (20% martensite) could be drawn to more than 6.06 total strain, while 0.1/IA/20 (20% martensite) failed after $\varepsilon=5.07$ [35]. This corresponds to the observed lower void density of 0.1/IQ/30 than 0.1/IA/30.

## 4.3. Fatigue of wires

### 4.3.1. Comparison of fatigue limits for IQ and IA

The S/N plots obtained for 0.1/IQ/30 and 0.1/IA/30 are presented in Figure 17. The fatigue limit, $\sigma_e$, for both 0.1/IQ/30 and 0.1/IA/30 is ~400 MPa (R=0.05) or ~600 MPa (R=-1) which is between 25 and 30% of the ultimate tensile strength. The limit for 0.1/IA/30 appears to be slightly higher than that for 0.1/IQ/30, but not significantly. The similar behavior of the drawn wires was expected, since the structures both consist of elongated martensite fibers in ferrite. The morphological differences between undrawn 0.1/IQ/30 and 0.1/IA/30 vanish after drawing, as do the effects of these differences.

The effect of the different initial martensite morphologies in undrawn structure was studied on the same silicon containing alloys by Dutta et al. [48]. The fatigue of 0.1/IQ/58 and 0.1/IA/44 (44% martensite) were tested and the threshold $\Delta K_0$ values were fount to be 10.7 MPa$\sqrt{m}$ and 19.5 MPa$\sqrt{m}$, respectively, when tested at R=0.05. The significantly higher $\Delta K_0$ value for 0.1/IA/44 was attributed to higher degree of roughness caused by the coarser microstructure, as verified by macroscopic crack closure measurements. The high fatigue resistance of as heat-treated dual-phase steels is due to the meandering of the crack path, which reduces crack growth rates by crack deflection and consequent roughness-induced crack closure mechanisms. The fatigue crack in undeformed dual-phase structures deflected extensively at ferrite/ferrite and ferrite/martensite interfaces. The crack closure and deflection caused by the meandering of the crack, which lower the stress intensity at the crack tip, are extrinsic toughening mechanisms. Intrinsic mechanisms, conversely, toughen by increasing the inherent crack growth resistance of the microstructure [48]. Shang et al. [20] investigated the relative contributions of extrinsic and intrinsic toughening in dual-phase steels by examining long and small crack growth. It was found that the extrinsic and intrinsic mechanisms compete; the structure with the highest long crack growth resistance has the lowest initiation and small crack growth resistance.

Recent fatigue studies on stress-relieved pearlitic wire drawn to $\varepsilon=2.36$ gave the fatigue limit as $\sigma_e=503$ MPa (R=-1) which was 24% of the ultimate tensile strength [**28**]. Eliminating the residual tensile stresses on the wire surface increases the fatigue limit, so the results of the dual-phase and pearlitic steel wire tests may not strictly be compared. However, even with the benefit of stress-relieving, the pearlitic wires had a lower endurance ratio. Since the wires in both investigations were tested in the unpolished condition, the specimen lifetime represented only the propagation of the fatigue crack, since drawing introduces enough defects as to make the time to initiate a small crack negligible. The dual-phase wire, then, has a higher resistance to crack propagation than pearlitic wire.

### 4.3.2. Crack initiation sites

Most failures initiated at inclusions or holes left by inclusions at the wire surface (Figure 18a). Failure was also observed to have started from a crack at the wire surface (Figure 18b) which may have formed in one of two ways: a martensite grain which may have broken during drawing, or a void which formed at the end of a martensite particle during drawing. Geometrically, the shear crack through a martensite particle is more likely to have initiated the void. Fatigue cracks which initiate at voids formed during wire drawing can be reduced by forming wires from intermediately quenched material. One failure was caused by an internal defect (Figure 18c): a crack formed during drawing was responsible for the failure. Cracks initiated at the intersection of two grooves formed during drawing were not observed, contrary to the findings of Verpoest [**28**]. A statistically correct study of the percentage of failures caused by the different observed initiators for wires drawn from various starting structures would require more testing than was done for this investigation.

### 4.3.3. Fatigue fracture surface

Typical fatigue fracture surfaces of 0.1/IQ/30 and 0.1/IA/30 specimens tested at the same mean and amplitude stresses are compared in Figures 19-21. Both exhibited classic features such as the semicircular fatigue zone about the surface initiation site, and a ductile fast fracture zone. The fatigue zone was subdivided into three regions of differing roughness. Near the initiation site, the surface was very smooth and flat. Then, beach marks become observable, increasing in roughness as the distance from the initiation site increases. The beach marks are not continuous and are often hard to define near internal cracks. The third region was one of more roughness near the fast fracture zone.

The fracture surfaces were also examined in longitudinal cross-section (Figures 22-24). The fatigue zone was nearly linear and normal to the loading direction. There was no significant deflection at grain boundaries, as in the as-heat-treated samples. This is probably because the ferrite has been hardened by drawing to such a degree that the crack is less sensitive to the difference between the ferrite and martensite phases. This corresponds to the work-hardening behavior at high tensile strains: when the martensite phase begins to deform, the work-hardening rate became insensitive to the martensite volume fraction.

### 4.3.4. Small crack growth

The fatigue cracks in wires of diameter 0.055 in (1.2 mm) satisfy the definition of physically small cracks (cracks less than 0.5 to 1 mm) [**49**]. To study the small crack behavior in dual-phase wires, crack initiation and early growth was monitored by replication [**20, 50**]. Although the use of cellulose-acetate strips has worked on four-point bend tests, it was neither sensitive enough nor reliable enough to yield sufficient small crack data. The crack was almost always indistinguishable even though the wires were fatigued nearly to failure. To make location of the replicated crack easier to determine and the surface was replicated in duplicate since half the wire surface was duplicated with each of four strips, rotating 90° between applications.

The failure of this technique could have been due to operator error or to non-applicability of the replication method to wires of fine diameter. If the wires had been larger in diameter, the cellulose-acetate tapes may have been more able to replicate small cracks. A machine problem that was encountered was that an overload was occasionally occasionally applied to the the sample when the test was interrupted to replicate the wire surface. The CRT trace and load-displacement output from the machine were not sensitive enough to indicate the transient effects. However, some samples which were replicated never failed in $10^6$ cycles at loads which should have caused failure at 2 or 3 orders of magnitude fewer cycles. A single overload of sufficient magnitude would create a plastic zone ahead of the crack tip large enough to prevent failure.

### 4.3.5. Softening during fatigue

The drawn structure after cyclic loading exhibits considerable roughening of the ferrite/martensite interface, more for 0.1/IQ/30 than 0.1/IA/30 (Figure 25), due to the softening of the structure during fatigue. Low carbon steel wires were found to soften during fatigue by Min et al. [**51**]. Wires drawn to true strain $\varepsilon=2.59$ initially had fine grains elongated in the drawing direction with a high density of dislocations inside the subgrains. During cyclic loading, the dislocation density in the interior of the grains decreased due to dynamic recovery: the cells became coarser and more equiaxed in the longitudinal direction, and slip bands probably formed. The formation of slip bands would explain the steps on the ferrite/martensite interface; TEM is required to verify their existence, however. The softening during fatigue might increase the plastic zone size sufficiently to cause the reappearance of crack closure.

## 5. CONCLUSIONS

Based on a study of the mechanical properties of drawn dual-phase steel wires the following conclusions may be stated:

1. The initial work-hardening rate increased with increased martensite volume fraction and strength. Highest work-hardening rates are achieved with incoherent ferrite/martensite interfaces.

2. The wire drawing limit is postponed by discouraging void formation at ferrite/martensite interfaces and through martensite particles. Void density is low in structures with lath martensite, which has a coherent interface with the ferrite matrix.

3. Fatigue cracks in drawn wires initiated at inclusions, decohesion sites, or fractured martensite particles on the surface of the wire. Large cracks in the interior of the wire also acted as crack initiators. The resistance to crack initiation may be increased by reducing inclusion density and by discouraging void formation in the wire.

4. The fatigue limit of drawn dual-phase wire is 25-30% of the ultimate tensile strength. Although the fatigue limit increased with drawing strain, the ultimate tensile strength increased faster, which resulted in a lower ratio of the two stresses. The excellent fatigue crack resistance of pre-drawn dual-phase steel is due mainly to crack path meandering, which is eliminated in small wires. The differences in starting morphology are minimized during drawing and so have little effect on fatigue properties.

5. The fatigue resistance of dual-phase wires is superior to that of pearlitic steel wire drawn to the same strain.

## 6. ACKNOWLEDGEMENTS

I am indebted to Prof. Gareth Thomas for the opportunity to perform this research and for his direction and support. Prof. Robert O. Ritchie provided valuable advice on fatigue and fracture analysis. I am grateful to Dr. Leposava Sidjanin for instruction in failure analysis and for her innumerable suggestions. Prof. Frank E. Hauser reviewed this manuscript and made helpful comments.

The technical assistance of many people made this investigation possible. I would especially like to thank Weyland Wong for hours of instruction in machining and mechanical testing, James Wu and John Holthuis for assistance in rolling rods, Wei Kang Yu for advice on fatigue testing and analysis, and Adrian Gronsky for instruction in operating a transmission electron microscope. Thanks are also due to Herb Riebe for instruction in machining, Felix Norris for help in operating the Instron.

Larry Edelson was a soundingboard in all phases of my work; this thesis would not exist but for all the support he has given.

This work was supported by the Director, Office of Energy Research, Office of Basic Energy Sciences, Materials Sciences Division of the U.S. Department of Energy under Contract No. DE-AC03-76SF00098.

## 7. REFERENCES

1. J. Y. Koo and G. Thomas, "Thermal Cycling Treatments and Microstructures for Improved Properties," *Mater Sci Eng*, 24 (1976) 187-198.

2. S. Hayami and T. Furukawa, "Micro Alloying '75," Proceedings of an International Symposiom on High Strength Low Alloy Steels, (1977) 311-321.

3. Formable HSLA and Dual-Phase Steels, A. T. Davenport (ed), TMS-AIME, Warrendale, PA (1979).

4. Dual Phase and Cold Pressing Vanadium Steels in the Automobile Industry, Vanitec, Berlin, W. Germany (1978).

5. Structure and Properties of Dual-Phase Steels, R. A. Kot and J. W. Morris (eds), TMS-AIME, Warrendale, PA (1979).

6. Fundamentals of Dual-Phase Steels, R. A. Kot and B. L. Bramfitt (eds), TMS-AIME, Warrendale, PA (1981).

7. Metallurgy of Continuously-Annealed Sheet Steel, B. L. Bramfitt and P. L. Mangonon, Jr (eds), TMS-AIME, Warrendale, PA (1981).

8. M. R. Plichta and H. I. Aaronson, "Influence of Alloying Elements upon the Morphology of Austenite Formed from Martensite in Fe-C-X Alloys," *Metall Trans*, 5 (1974) 2611-2613.

9. C. I. Garcia and A. J. De Ardo, "Formation of Austenite in 1.5 Pct Mn Steels," *Metall Trans A*, 12 (1981) 521-530.

10. G. R. Speich, V. A. Demarest and R. L. Miller, "Formation of Austenite During Intercritical Annealing of Dual-Phase Steels," *Metall Trans A*, 12 (1981) 1419-1428.

11. T. Tanaka, N. Tabata, T. Hatomura and C. Shiga, "Three Stages of the Controlled-Rolling Process," Micro-Alloying 75, Union Carbide Corp, New York, NY (1977).

12. R. Priestner and E. de los Rios, "Ferrite Grain Refinement by Controlled Rolling of Low-Carbon and Microalloyed Steel," *Met Tech* (1980) 309-316.

13. G. Thomas, Frontiers in Materials Techniques, M. A. Meyers and O. T. Inal (eds), Elsevier Science Publishers B. V., The Netherlands (1985) 89-123.

14. A. H. Nakagawa and G. Thomas, "Microstructure-Mechanical Property Relationships of Dual-Phase Sreel Wire,"*Metall Trans A*, 16 (1985) 831-840.

15. J. Ahn and G. Thomas, Conference Proceedings of 57th Annual Convention/Interwire 85, Wire Association International, Guilford, CT, (1985), 55-61.

16. G. Thomas, "Design of Dual Phase Steels for Bars and Rods," presented at the International Symposium on Microalloying and New Processing Approaches for Bar and Forging Steels, July 8-10, 1986, Colorado School of Mines, Golden, CO.

17. D. A. Korzekwa, R. D. Lawson, D. K. Matlock and G. Krauss, "A Consideration of Models Describing the Strength and Ductility of Dual-Phase Steels," *Scr Metall*, 14 (1980) 1023-1028.

18. H. Suzuki and A. J. McEvily, "Microstructural Effects on Fatigue Crack Growth in a Low Carbon Steel," *Metall Trans A*, 10 (1979) 475-481.

19. K. Minakawa, Y. Matsuo and A. J. McEvily, "The Influence of a Duplex Microstructure in Steels on Fatigue Crack Growth in the Near-Threshold Region," *Metall Trans A*, 13 (1982) 439-445.

20. J. K. Shang, J. L. Tzou and R. O. Ritchie, "Role of Crack Tip Shielding in the Initiation and Growth of Long and Small Fatigue Cracks in Composite Microstructures," *Metall Trans A*, 18 (1987) 1613-1627.

21. K. Minakawa and A. J. McEvily, " On Crack Closure in the Near Threshold Region, *Scr Metall*, 15 (1981), 633-636.

22. S. Suresh, "Crack Deflection: Implications for the Growth of Long and Short Fatigue Cracks," *Metall Trans A*, 14 (1983) 2375-2385.

23. J. Wasynczuk, R. O. Ritchie and G. Thomas, "Effects of Microstructure on Fatigue Crack Growth in Duplex Ferrite-Martensite Steels," *Mater Sci Eng*, 62 (1984) 79-92.

24. Y. Tomota, "Effects of Morphology and Strength of Martensite on Cyclic Deformation Behaviour in Dual-Phase Steels," *Mat Sci Tech*, 3 (1987) 415-421.

25. J. DeMeyer, "Mechanische Eigenschappen van Tweefazen Staaldraad," M.S. Thesis, Katholieke Universiteit Leuven, Belgium (1984).

26. W. Zhongguang, W. Guonan, K. Wei, H. Haicai, "Influence of the Martensite Content on the Fatigue Behavior of a Dual-Phase Steel," *Mater Sci Eng*, 91 (1987) 99-144.

27. C. M. Wan, K. C. Chou, M. T. Jahn and S. M. Kuo, "Fatigue Studies on Dual-Phase Low Carbon Steel," *J Mat Sci*, 16 (1981) 2521-2526.

28. I. Verpoest, "The Fatigue Threshold, the Surface Condition and the Fatigue Limit of Steel Wire," Academiae Analecta, Belgium, 4 (1984) 17-56.

29. M. R. Mitchell, "Fundamentals of Modern Fatigue Analysis for Design," Fatigue and Microstructure, ASM (1979) 385-437.

30. Z. H. Min, L. Delaey and A. Deruyttere, "Fatigue Softening of Severely Cold-Drawn Low Carbon Steel," *Acta Metall*, 33 (1985) 563-570.

31. R. G. Davies and C. L. Magee, *ref 5*, 1-19.

32. W. R. Cribb and J. M. Rigsbee, "Work-Hardening Behavior and its Relationship to Microstrucutre and Mechanical Properties of Dual-Phase Steels," *ibid 5*, 91-117.

33. Y. Tomota, K. Kuroki, Mori and Tamura, "Tensile Deformation of Two-Ductile Phase Alloys: Flow Curves of $\alpha-\gamma$ Fe-Cr-Ni Alloys," *Mater Sci Eng*, 24 (1976) 85-94.

34. J. M. Rigsbee and P. J. VanderArend, "Laboratory Studies of Microstructures and Structure-Property Relationships in 'Dual-Phase' HSLA Steels," *ref 2*.

35. J. H. Ahn, "Design of Low Carbon Dual-Phase Steels for High Strength Wire," PhD Thesis, University of California, Berkeley, LBL-22591 (1986).

36. G. Langford, P. K. Nagata, R. J. Sober and W. C. Leslie, "Plastic Flow in Binary Substitutional Alloys of B.C.C. Iron--Effects of Wire Drawing and Alloy Content on Work Hardening and Ductility," *Metall Trans A*, 3, (1972) 1843-1849.

37. B. V. Narasimha Rao, "On the Orientation Relationships Between Retained Austenite and 'Lath' Martensite," *Metall Trans A*, 10 (1979) 645-648.

38. B. Karlsson and G. Linden, "Plastic Deformation of Ferrite-Pearlite Structures in Steel," *Mater Sci Eng*, 17 (1975) 209-219.

39. P. Priestner and C. L. Aw, "On Initial Yielding in Dual-Phase Steel," *Scr Metall* , 18 (1984) 133-136.

40. J. Y. Koo and G. Thomas, "Design of Duplex Low Carbon Steels for Improved Strength:Weight Applications," *ref 3*, 40-57.

41. J. Y. Koo and G. Thomas, Proc. 35th Annual Meeting EMSA, Baton Rounge, LA (1977) 118.

42. S. K. Das and G. Thomas, "On the Morphology and Substructure of Martensite," *Metall Trans*, 1 (1970) 325.

43. M. S. Rashid and B. V. N. Rao, "Tempering Characteristics of a Vanadium Containing Dual Phase Steel," *Metall Trans A*, 13A (1982) 1679-1686.

44. H. Y. Chang, R. K. Viswanadham and C. A. Wert, "Age-Hardening in the V-C and Nb-C Systems," *Metall Trans*, 5 (1974) 1907-1917.

45. R. H. Hoel and G. Thomas, "Ferrite Structure and Mechanical Properties of Low Alloy Duplex Steels," *Scr Metall*, 15 (1981) 867-872.

46. G. R. Speich, A. J. Schwoeble and G. P. Huffman,"Tempering of Mn and Mn-Si-V Dual-Phase Steels," *Metall Trans A*, 14 (1983) 1079-1081.

47. L. Sidjanin, S. Miyasato and G. Thomas, "Fracture Analysis of Drawn Composite Dual-Phase Steel Wire," Conf. Proc. of 57th Annual Convention/Interwire 87, Wire Association International, Guilford, CT (1987) 70-75.

48. V. B. Dutta, S. Suresh and R. O. Ritchie, "Fatigue Crack Propagation in Dual-Phase Steels: Effects of Ferritic-Martensitic Microstructures on Crack Path Morphology," *Metall Trans A*, 15 (1983) 1193-1207.

49. S. Suresh and R. O. Ritchie, "Propagation of Short Fatigue Crack," *Int Met Rev* , 29 (1984) 445-476.

50. R. O. Ritchie and J. Lankford,"Small Fatigue Cracks: a Statement of the Problem and Potential Solutions, *Mater Sci Eng* , 84 (1984) 11-16.

Chemical Composition
wt %

| | C | Si | Mn | P | S | Sol. Al | N | V |
|---|---|---|---|---|---|---|---|---|
| 0.2 | 0.215 | 2.09 | 0.28 | 0.005 | 0.0056 | 0.034 | 0.0027 | --- |
| 0.1 | 0.104 | 2.08 | 0.29 | 0.005 | 0.0049 | 0.035 | 0.0021 | --- |
| 0.05 | 0.053 | 2.06 | 0.28 | 0.005 | 0.0048 | 0.034 | 0.0021 | --- |
| 0.1/V | 0.10 | 1.74 | 0.009 | 0.005 | <0.005 | 0.01 | 0.0021 | 0.09 |

## Heat Treatment Properties

| | alloy | heat treatment process | temper? | anneal temp C | %M | %C in mart |
|---|---|---|---|---|---|---|
| 0.2/IQ/20 | 0.2 | IQ | --- | 775 | 20 | 0.96 |
| 0.2/IQ/30 | 0.2 | IQ | --- | 800 | 30 | 0.64 |
| 0.1/IQ/30 | 0.1 | IQ | --- | 940 | 30 | 0.33 |
| 0.1/IA/30 | 0.1 | IA | --- | 940 | 30 | 0.33 |
| 0.05/IQ/30 | 0.05 | IQ | --- | 1025 | 30 | 0.17 |
| 0.05/IQ/40 | 0.05 | IQ | --- | 1045 | 40 | 0.12 |
| 0.1/V/IQ/20 | 0.1/V | IQ | --- | 920 | 20 | 0.50 |
| 0.1/V/IQT/20 | 0.1/V | IQ | yes | 920 | 20 | 0.50 |
| 0.1/V/CR/20 | 0.1/V | CR | --- | 950 | 20 | 0.50 |
| 0.1/V/CRT/20 | 0.1/V | CR | yes | 950 | 20 | 0.50 |

## Tensile Properties

| | YS | | UTS | | $\varepsilon_u$ | $\varepsilon_t$ | RA |
|---|---|---|---|---|---|---|---|
| | ksi | MPa | ksi | MPa | % | % | % |
| 0.2/IQ/20 | 79 | 545 | 140 | 965 | 10.1 | 20.2 | 47 |
| 0.2/IQ/30 | 93 | 641 | 161 | 1110 | 11.9 | 14.9 | 21 |
| 0.1/IQ/30 | 75 | 517 | 132 | 910 | 11.2 | 20.7 | 59 |
| 0.1/IA/30 | 78 | 108 | 131 | 904 | 8.8 | 16.4 | 43 |
| 0.05/IQ/30 | 72 | 496 | 111 | 765 | 10.4 | 21.8 | 66 |
| 0.05/IQ/40 | 77 | 531 | 118 | 814 | 8.3 | 20.2 | 67 |
| 0.1/V/IQ/20 | 75 | 519 | 122 | 843 | 8.9 | 18.5 | 49 |
| 0.1/V/IQT/20 | 68 | 472 | 68 | 468 | 9.8 | 20.2 | 65 |
| 0.1/V/CR/20 | 76 | 526 | 123 | 848 | 10.9 | 21.1 | 57 |
| 0.1/V/CRT/20 | 79 | 546 | 107 | 738 | 12.9 | 24.2 | 68 |

Work Hardening Rates

at true strain, $\varepsilon = 0.06$

| | work hardening rate | |
|---|---|---|
| | MPa | ksi |
| 0.2/IQ/20 | 12,100 | 1750 |
| 0.2/IQ/30 | 17,200 | 2490 |
| 0.1/IQ/30 | 13,700 | 1990 |
| 0.1/IA/30 | 19,400 | 2810 |
| 0.05/IQ/30 | 11,900 | 1720 |
| 0.05/IQ/40 | 13,100 | 1900 |
| 0.1/V/IQ/20 | 16,200 | 2350 |
| 0.1/V/IQT/20 | 13,400 | 1940 |
| 0.1/V/CR/20 | 15,800 | 2300 |
| 0.1/V/CRT/20 | 5,870 | 851 |

# Drawing Schedule

| Pass | Die Diameter<br>in | <br>mm | RA Per Pass<br>% | RA Total<br>% | Total<br>True Strain |
|---|---|---|---|---|---|
| --- | 0.166 | 4.20 | --- | --- | --- |
| 1 | 0.135 | 3.42 | 33.8 | 33.8 | 0.41 |
| 2 | 0.114 | 2.91 | 27.9 | 52.2 | 0.74 |
| 3 | 0.0979 | 2.49 | 26.8 | 65.0 | 1.05 |
| 4 | 0.0850 | 2.16 | 24.6 | 72.7 | 1.30 |
| 5 | 0.0745 | 1.89 | 23.2 | 79.7 | 1.60 |
| 6 | 0.0660 | 1.68 | 21.5 | 84.1 | 1.84 |
| 7 | 0.0600 | 1.52 | 17.4 | 86.9 | 2.03 |
| 8 | 0.0545 | 1.38 | 17.5 | 89.2 | 2.22 |

Tensile Properties of Drawn Wire

| | YS | | UTS | | $\varepsilon_t$ | RA |
|---|---|---|---|---|---|---|
| | ksi | MPa | ksi | MPa | % | % |
| 0.2/IQ/30 | --- | --- | 306 | 2110 | --- | 8.1 |
| 0.1/IQ/30 | 188 | 1300 | 277 | 1910 | 22 | 58 |
| 0.1/IA/30 | 202 | 1400 | 276 | 1900 | 11 | 54 |

Density of Voids

$mm^{-2}$

| | inclusions | normal decohesion | parallel decohesion | martensite shear crack | total | TOTAL (excluding inclusions) |
|---|---|---|---|---|---|---|
| 0.2/IQ/30 | 44 | 438 | 88 | 420 | 990 | 946 |
| 0.1/IQ/30 | 245 | 26 | 61 | 26 | 358 | 113 |
| 0.1/IA/30 | 210 | 140 | 79 | 53 | 482 | 272 |

# FIGURE CAPTIONS

Figure 1. Heat treatment schemes and resulting microstructures for intermediate quenching (IQ), intercritical annealing (IA), and controlled rolling (CR). IQ produced packets of parallel martensite fibers in a continuous ferrite matrix. IA produced fine globular martensite at ferrite grain boundaries. CR produced fibrous martensite surrounded by equiaxed ferrite grains. [XBL 8711-4871]

Figure 2. Specifications for sub-size cylindrical tensile specimen. [XBL 8711-4995]

Figure 3. Grips used for testing wires 0.055 in (1.4 mm) in diameter in tension and fatigue. The grips were designed such that the load required to secure the sample in the grip gradually decreases to help prevent failure at the mouth. [XBL 8711-4996]

Figure 4. SEM micrographs of the microstructures produced by: (a) intermediate quenching (IQ), (b) intercritical annealing (IA), and (c) controlled rolling (CR). Martensite phase is in light contrast. [XBB 878-7439A, XBB 878-7032A]

Figure 5. TEM bright field image of twin-related lath martensite (dark thin grain) in 0.2/IQ/30. [XBB 870-9953]

Figure 6. TEM micrographs of twinned plate martensite in 0.2/IQ/30. (a) Bright field, (b) dark field, and (c) diffraction pattern showing the two martensite zones. [XBB 870-8587A]

Figure 7. TEM bright field image of lath martensite formed in 0.1/IQ/30. [XBB 870-9952]

Figure 8. TEM bright field image of lath martensite formed in 0.1/IA/30. [XBB 870-9951]

Figure 9. TEM of dislocated lath martensite. (a) Bright field image, (b) dark field image formed with the 002 austenite reflection, (c) selected area diffraction pattern showing the two martensite zones, and the zone of the retained austenite, and (d) indexed pattern. [XBB 870-8588]

Figure 10. TEM bright field image of fine vanadium carbides in ferrite produced in tempered control-rolled sample. Note the formation of precipitate-free zones at the grain boundaries. [XBB 870-9954]

Figure 11. Comparison of engineering stress-strain curves for control-rolled samples before and after tempering. Tempering results in the re-appearance of discontinuous yielding. [XBL 8711-4872]

Figure 12. SEM fractographs of tensile fracture surfaces of undrawn structures:
(a), (b) 0.1/V/CR/20
(c), (d) 0.1/V/CRT/20
Tempering increases the reduction in area in the neck. [XBB 878-7029A]

Figure 13. SEM micrographs of microstructures of wire drawn from (a) 0.2/IQ/30, (b) 0.1/IQ/30, and (c) 0.1/IA/30. Although all structures show elongated martensite grains, the martensite in 0.2/IQ/30 elongated to a lesser extent. [XBB 878-7027A]

Figure 14. Examples of voids observed in drawn wires:
(a) void about inclusion,
(b) decohesion of ferrite/martensite interface normal to the drawing direction caused by a dead zone at the end of the martensite grain,
(c) decohesion of ferrite/martensite interface parallel to the drawing direction,
(d) shear cracking of martensite particle.
[XBB 870-8534A, XBB 878-7020A]

Figure 15. SEM micrographs of the evolution of shear failure of the martensite phase during wire drawing. (a) is from an earlier drawing pass than (b). [XBB 878-7014A]

Figure 16. Tensile fracture surfaces of drawn wires produced by
(a), (b), (c) 0.2/IQ/30
(d), (e) 0.1/IQ/30
(f), (g) 0.1/IA/30. [XBB 870-8491A, XBB 870-8530A]

Figure 17. S/N curves for wires produced from 0.1/IQ/30 and 0.1/IA/30 indicates that the fatigue limit of 0.1/IA/30 may be slightly higher than 0.1/IQ/30. [XBL 8711-4873]

Figure 18. SEM micrographs of initiation sites for fatigue cracks were
(a) inclusions/holes at wire surface,
(b) decohesion of ferrite/martensite interface normal to the drawing load, or shear cracking of martensite particles,
(c) cracks in the interior of the wire which were formed during drawing.
[XBB 878-7018A, XBB 878-7011A]

Figure 19. Low magnification SEM of fatigue fracture surfaces of wires drawn from (a) 0.1/IQ/30 and (b) 0.1/IA/30. Initiation sites are indicated by arrows. Fatigue zone has the typical penny-shaped outline, and the fast fracture zone contains considerable secondary cracking. [XBB 870-8489A]

Figure 20. Higher magnification SEM of fatigue fracture surfaces of wires drawn from 0.1/IQ/30: (a) crack near initiation site, (b) mid-zone, (c) near end of zone, (d) ductile fast fracture. [XBB 870-8499A]

Figure 21. Higher magnification SEM of fatigue fracture surfaces of wire drawn from 0.1/IA/30: (a) crack near initiation site, (b) mid-zone, (c) near end of zone, (d) ductile fast fracture. [XBB 879-7362A]

Figure 22. Low magnification SEM of fatigue crack profile obtained by cutting fracture surface in half longitudinally for (a) 0.1/IQ/30, and (b) 0.1/IA/30. Little deflection of the crack is seen in either IQ or IA. [XBB 870-8893A]

Figure 23. Higher magnification SEM of fatigue crack profile of 0.1/IQ/30 (crack growth direction indicated by arrow): (a) near initiation site, (b) mid-zone, (c) near end of zone, (d) fast fracture. [XBB 870-8889A]

Figure 24. Higher magnification SEM of fatigue crack profile of 0.1/IA/30 (crack growth direction indicated by arrow): (a) near initiation site, (b) mid-zone, (c) near end of zone, (d) fast fracture. [XBB 870-8899A]

Figure 25. Scanning electron micrographs of martensite particles after cyclic loading for (a) 0.1/IQ/30, and (b) 0.1/IA/30. The degree of roughness at the martensite/ferrite interface is larger for IQ than IA. [XBB 870-8895A]

Figure 26. Dislocation model of shear cracking in martensite. [XBL 870-4277]

Heat Treatment Schedules

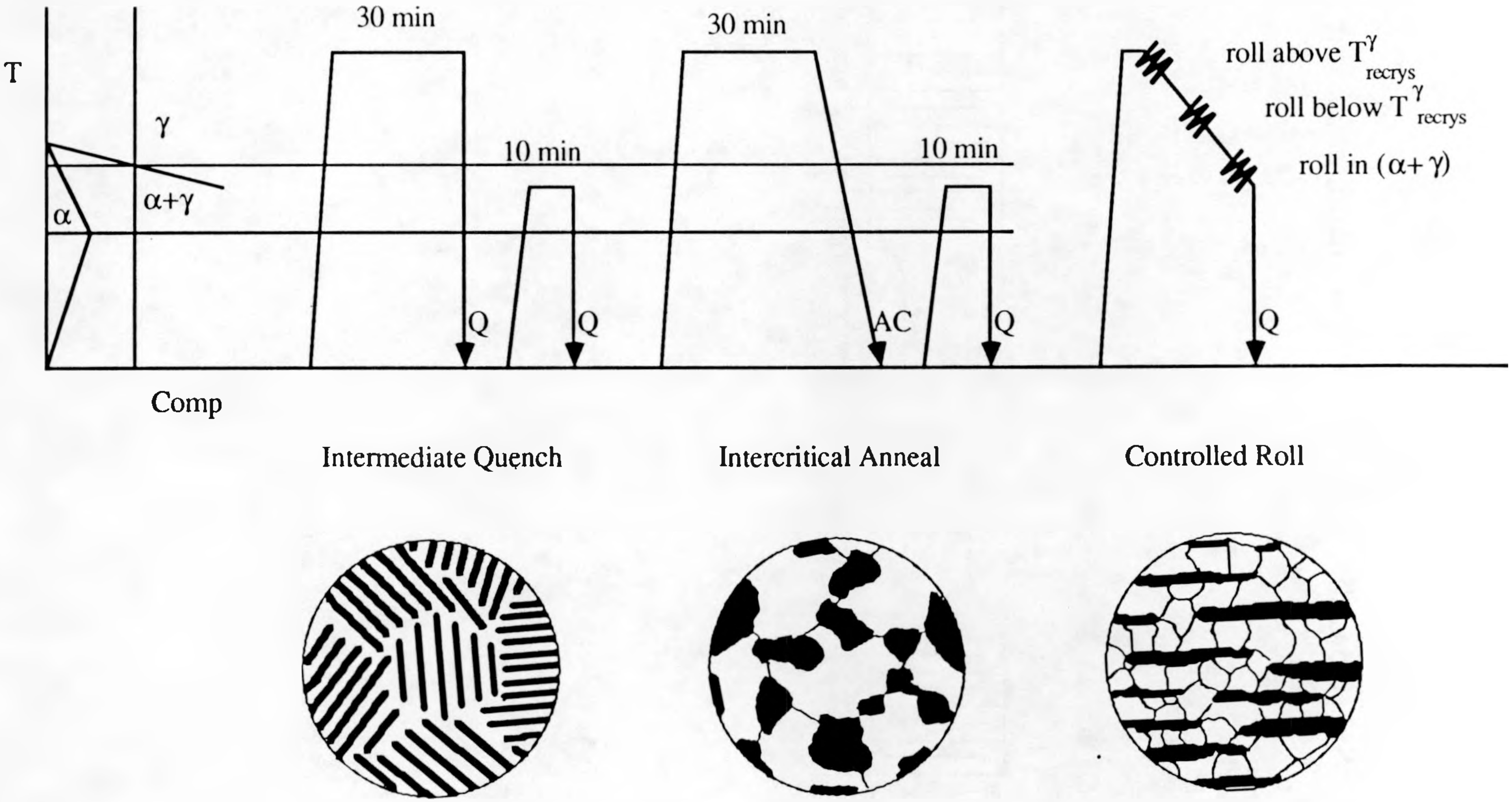

XBL 8711-4871

Subsize Cylindrical Tensile Specimen Dimensions

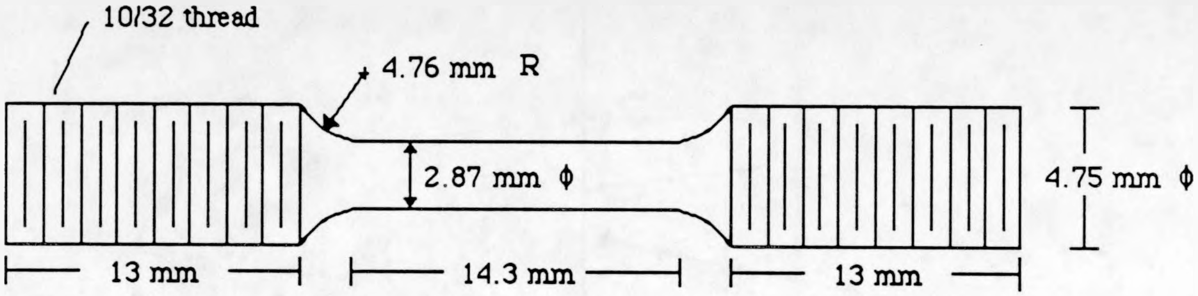

XBL 8711-4995

# Leafspring Grips

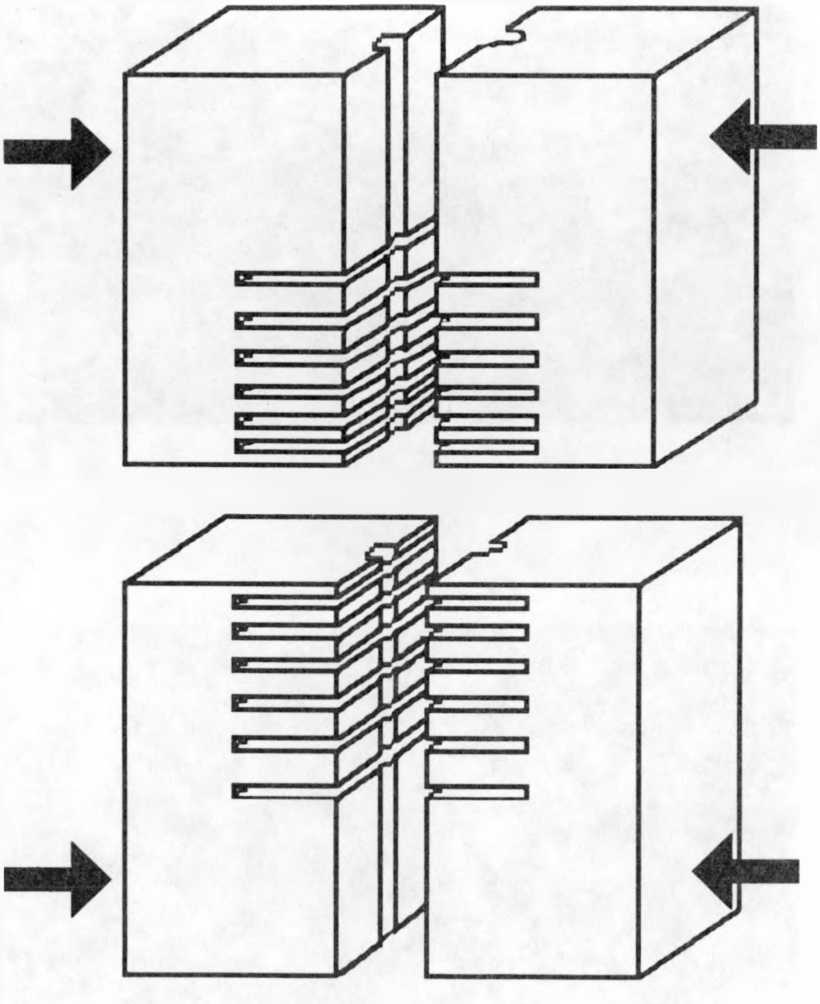

XBL 8711-4996

Figure 3. Grips used for testing wires 0.055 in (1.4 mm) in diameter in tension and fatigue. The grips were designed such that the load required to secure the sample in the grip gradually decreases to help prevent failure at the mouth.

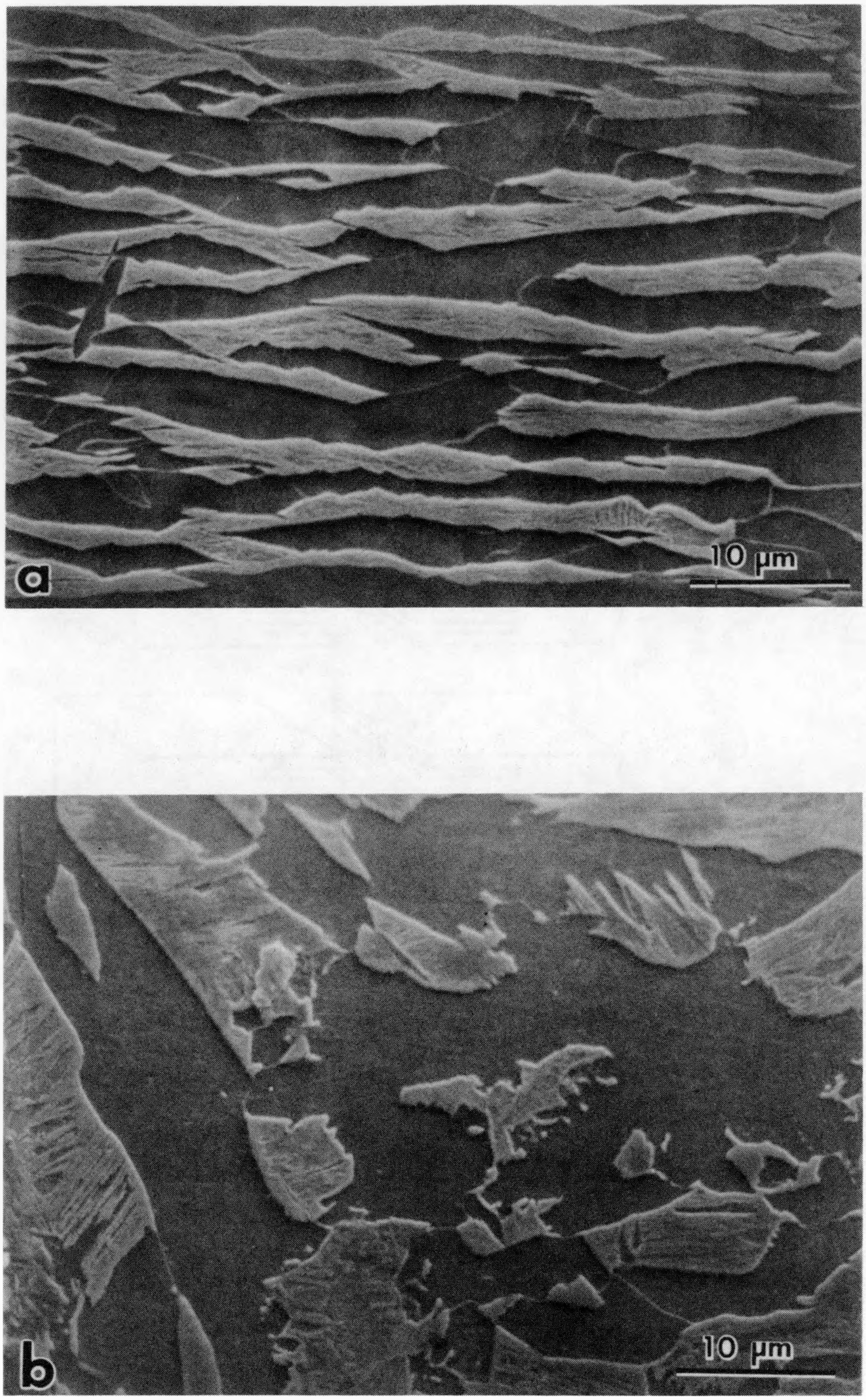

XBB 878-7439A

Figure 4. SEM micrographs of the microstructures produced by: (a) intermediate quenching (IQ), (b) intercritical annealing (IA), and (c) controlled rolling (CR). Martensite phase is in light contrast.

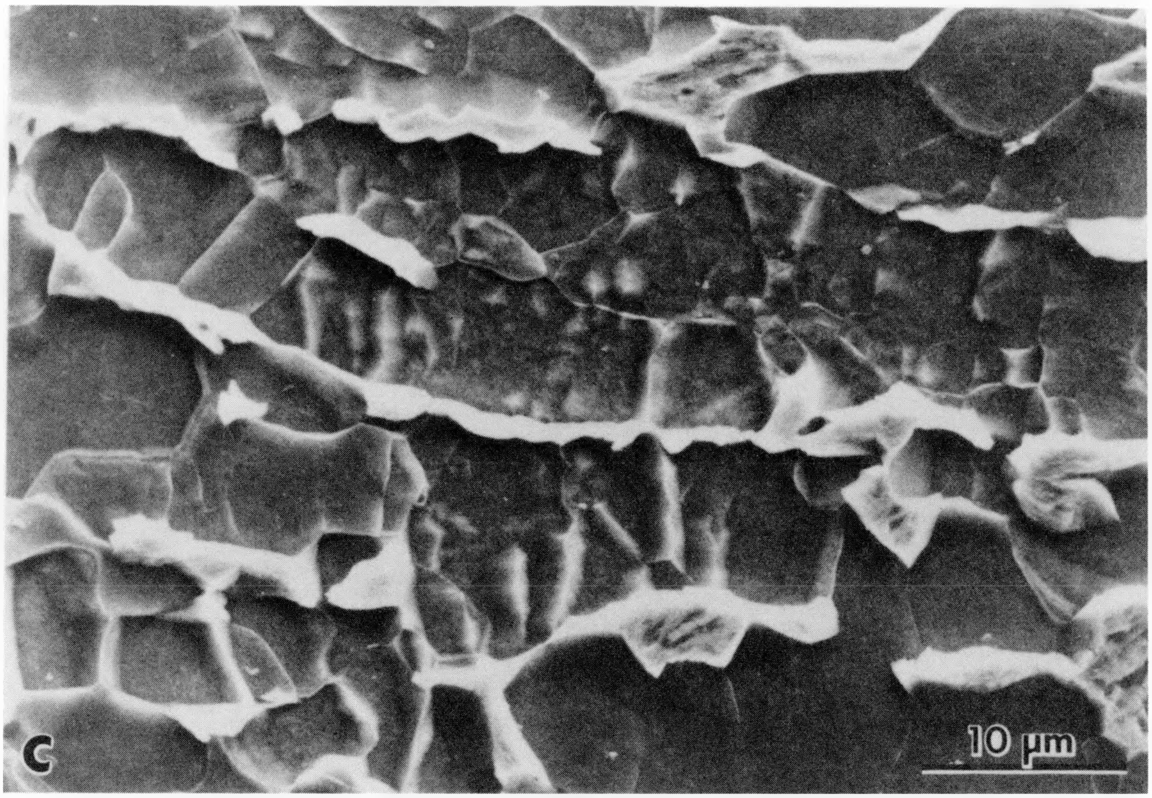

XBB 878-7032A

XBB 870-9953

Figure 5. TEM bright field image of twin-related lath martensite (dark thin grain) in 0.2/IQ/30.

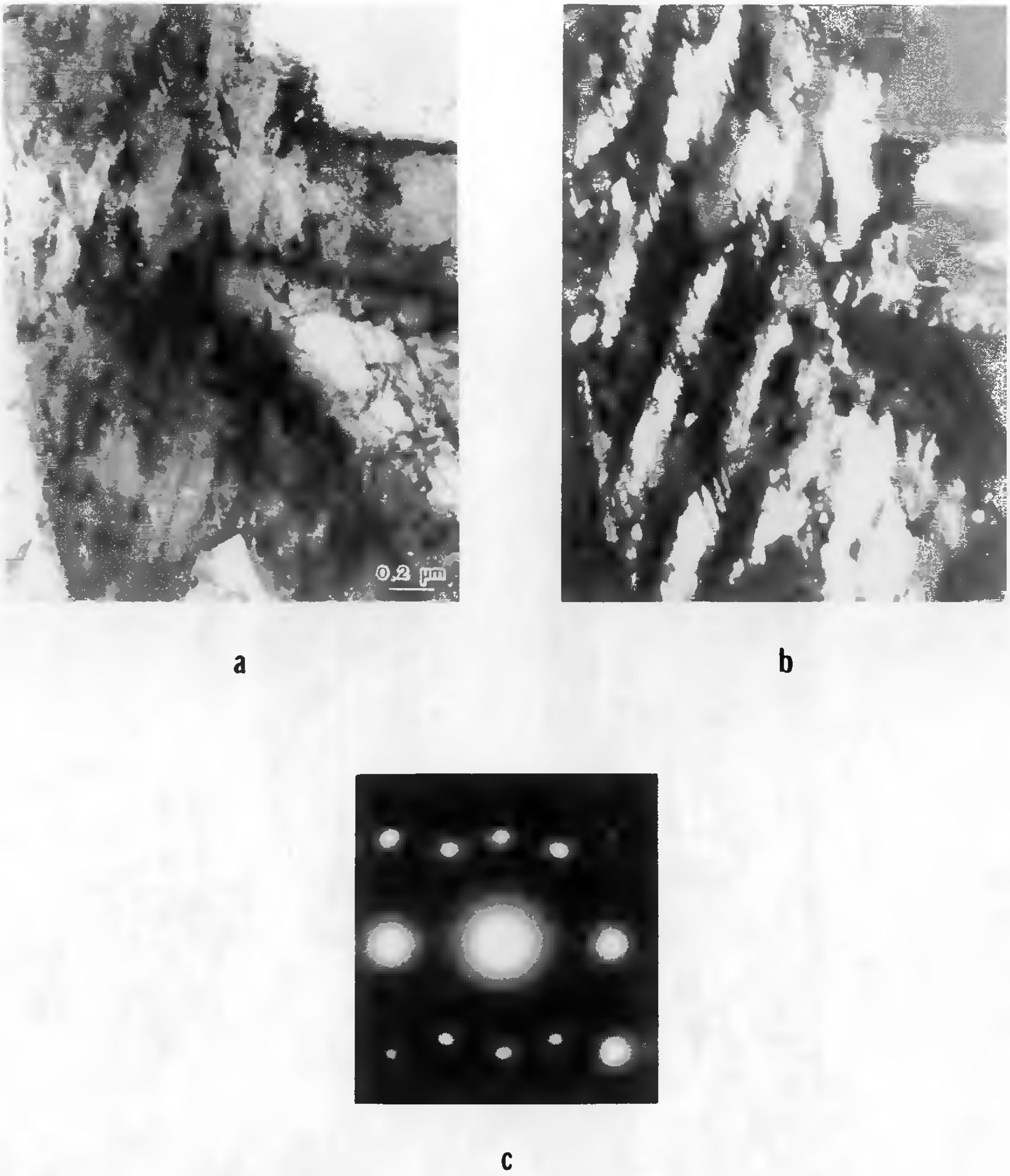

XBB 870-8587A

Figure 6. TEM micrographs of twinned plate martensite in 0.2/IQ/30. (a) Bright field, (b) dark field, and (c) diffraction pattern showing the two martensite zones.

XBB 870-9952

Figure 7. TEM bright field image of lath martensite formed in 0.1/IQ/30.

XBB 870-9951

Figure 8. TEM bright field image of lath martensite formed in 0.1/IA/30.

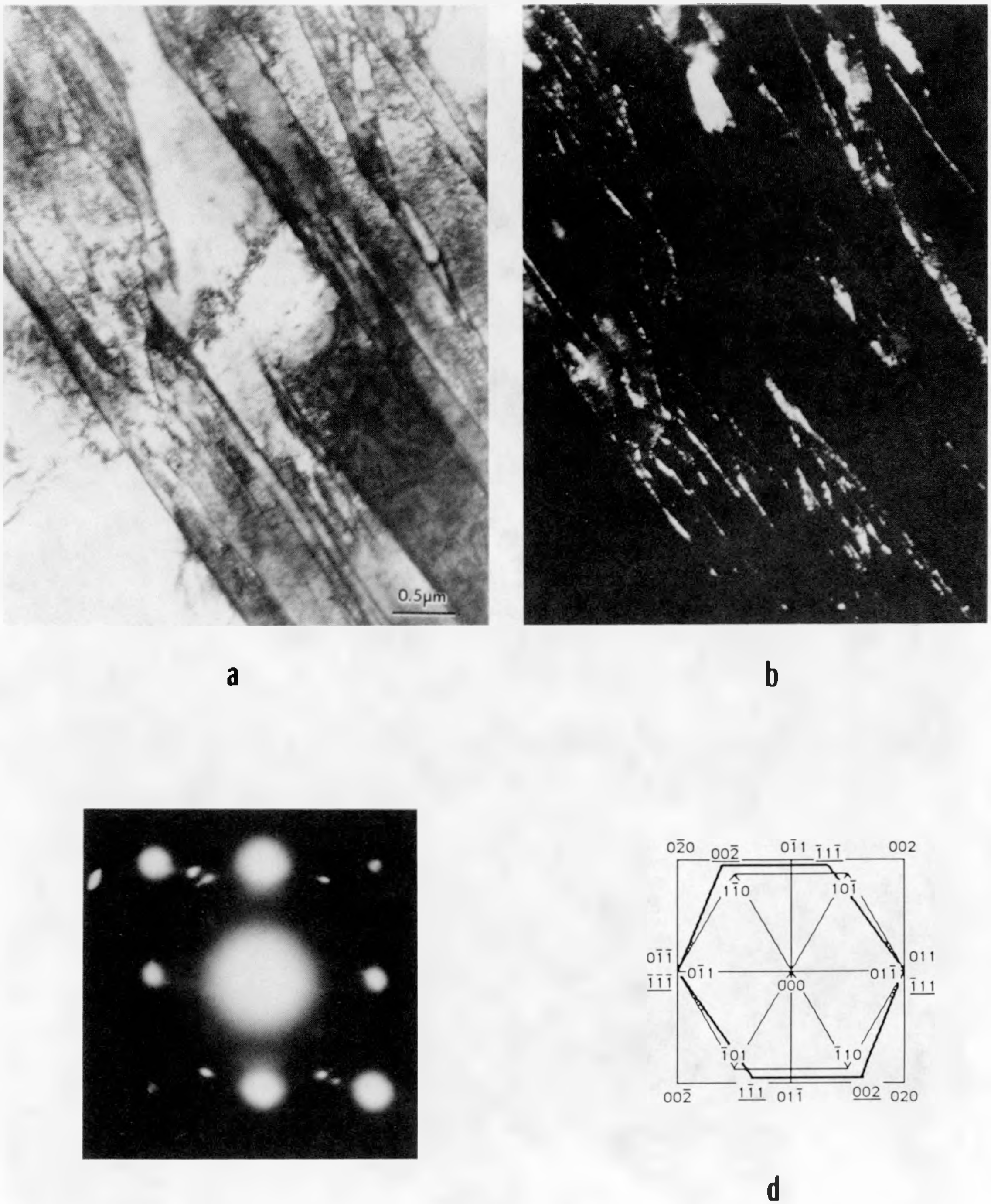

XBB 870-8588

Figure 9. TEM of dislocated lath martensite. (a) Bright field image, (b) dark field image formed with the 002 austenite reflection, (c) selected area diffraction pattern showing the two martensite zones, and the zone of the retained austenite, and (d) indexed pattern.

XBB 870-9954

Figure 10. TEM bright field image of fine vanadium carbides in ferrite produced in tempered control-rolled sample. Note the formation of precipitate-free zones at the grain boundaries.

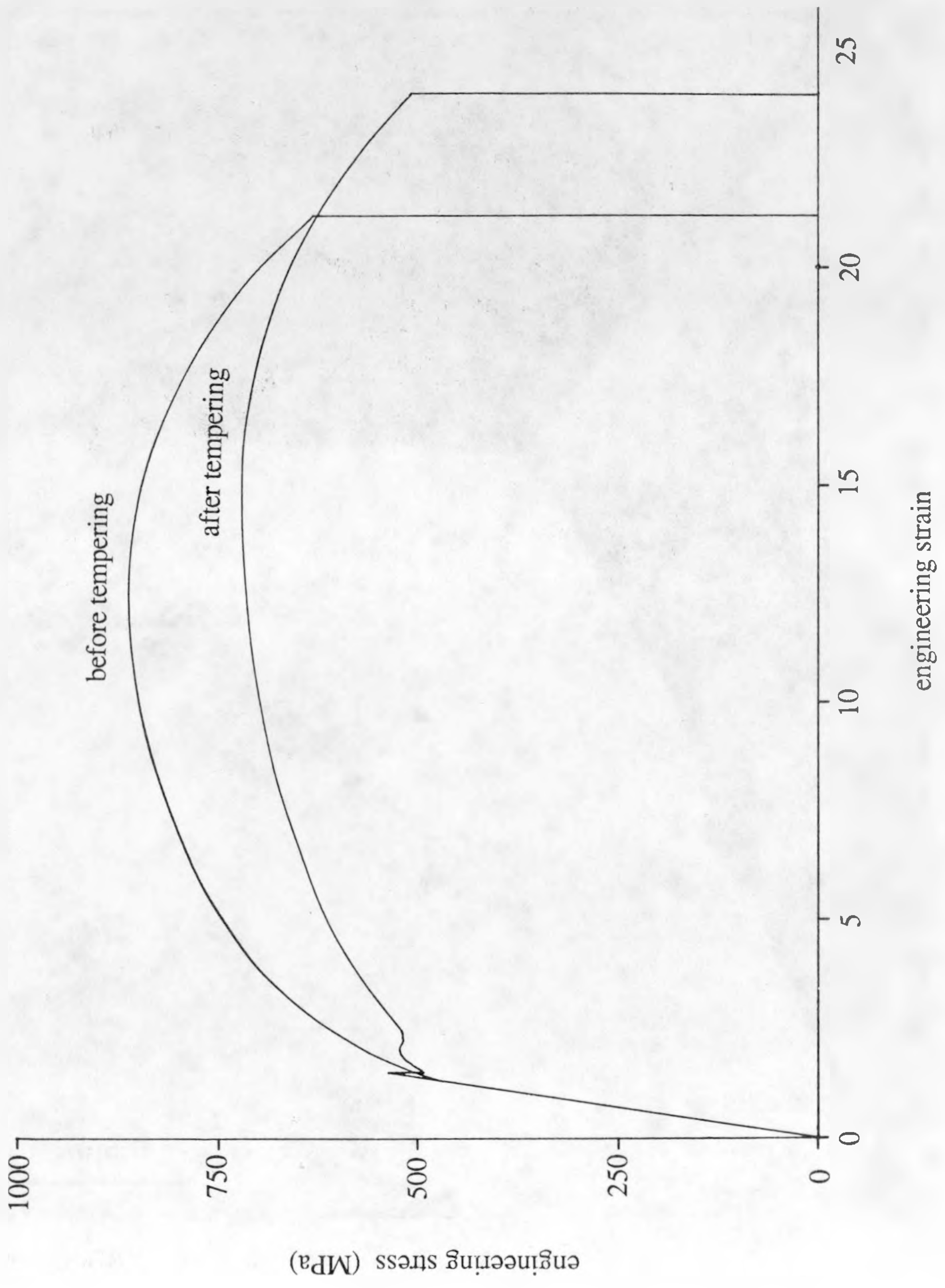

XBL 8711-4872

Figure 11. Comparison of engineering stress-strain curves for control-rolled samples before and after tempering. Tempering results in the re-appearance of discontinuous yielding.

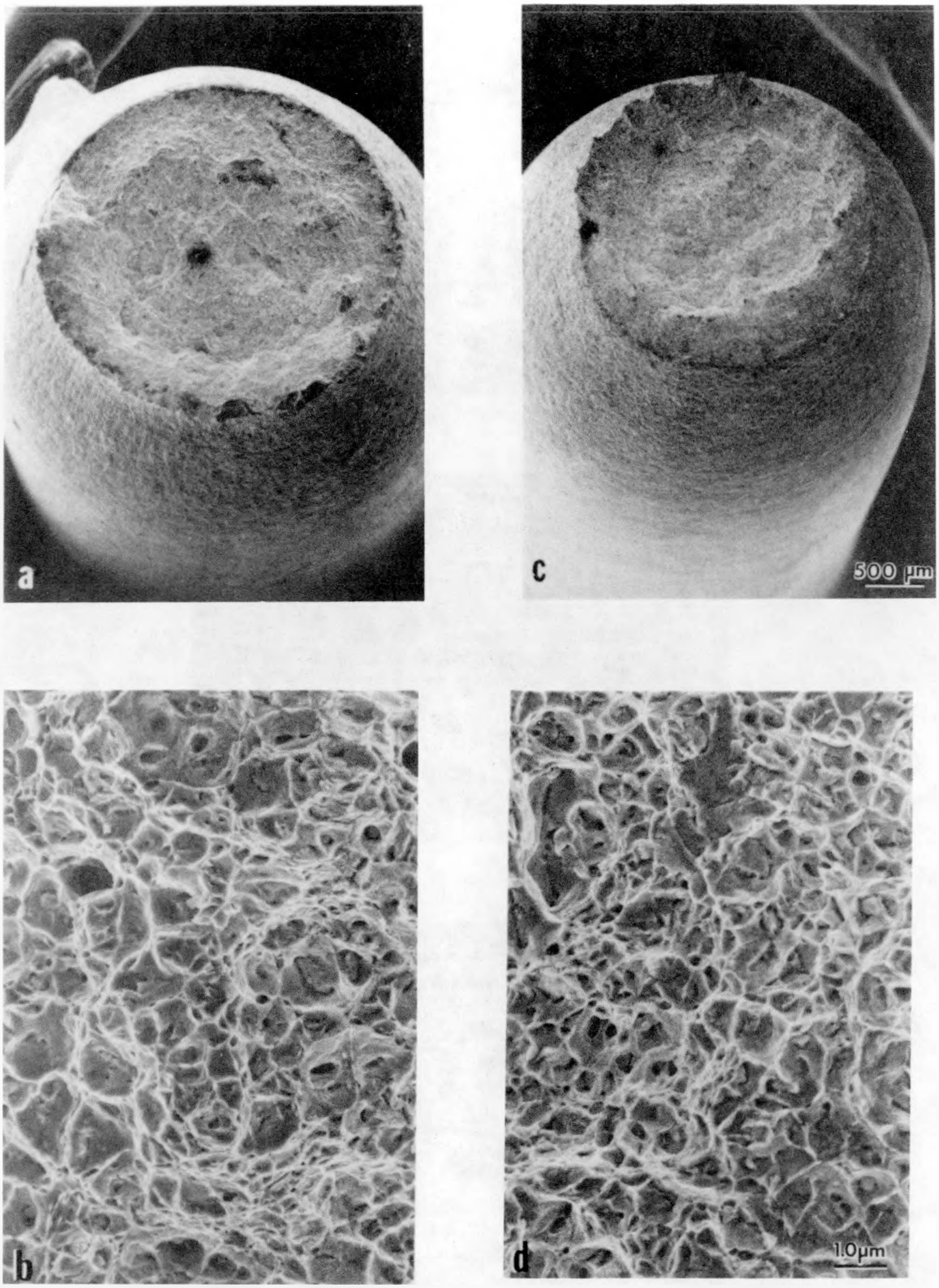

XBB 878-7029A

Figure 12. SEM fractographs of tensile fracture surfaces of undrawn structures:
(a), (b) 0.1/V/CR/20
(c), (d) 0.1/V/CRT/20
Tempering increases the reduction in area in the neck.

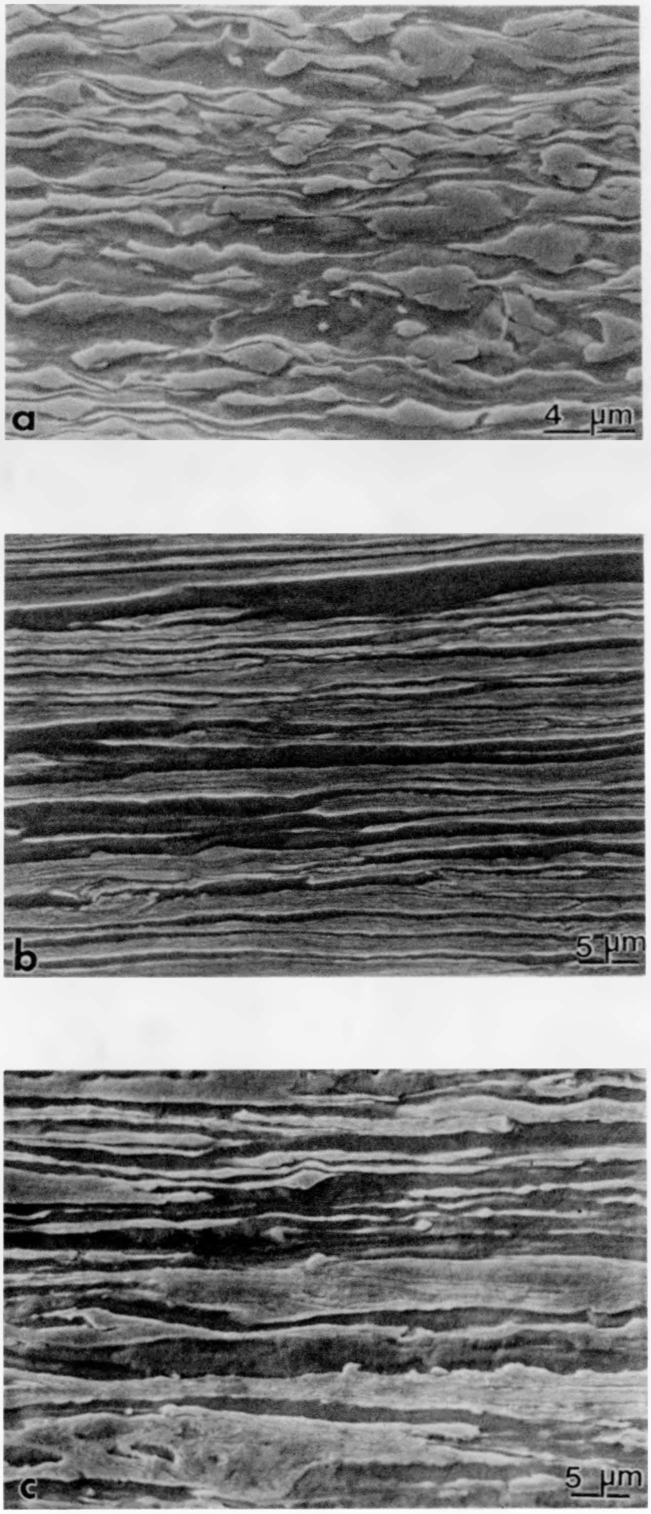

XBB 878-7027A

Figure 13. SEM micrographs of microstructures of wire drawn from (a) 0.2/IQ/30, (b) 0.1/IQ/30, and (c) 0.1/IA/30. Although all structures show elongated martensite grains, the martensite in 0.2/IQ/30 elongated to a lesser extent.

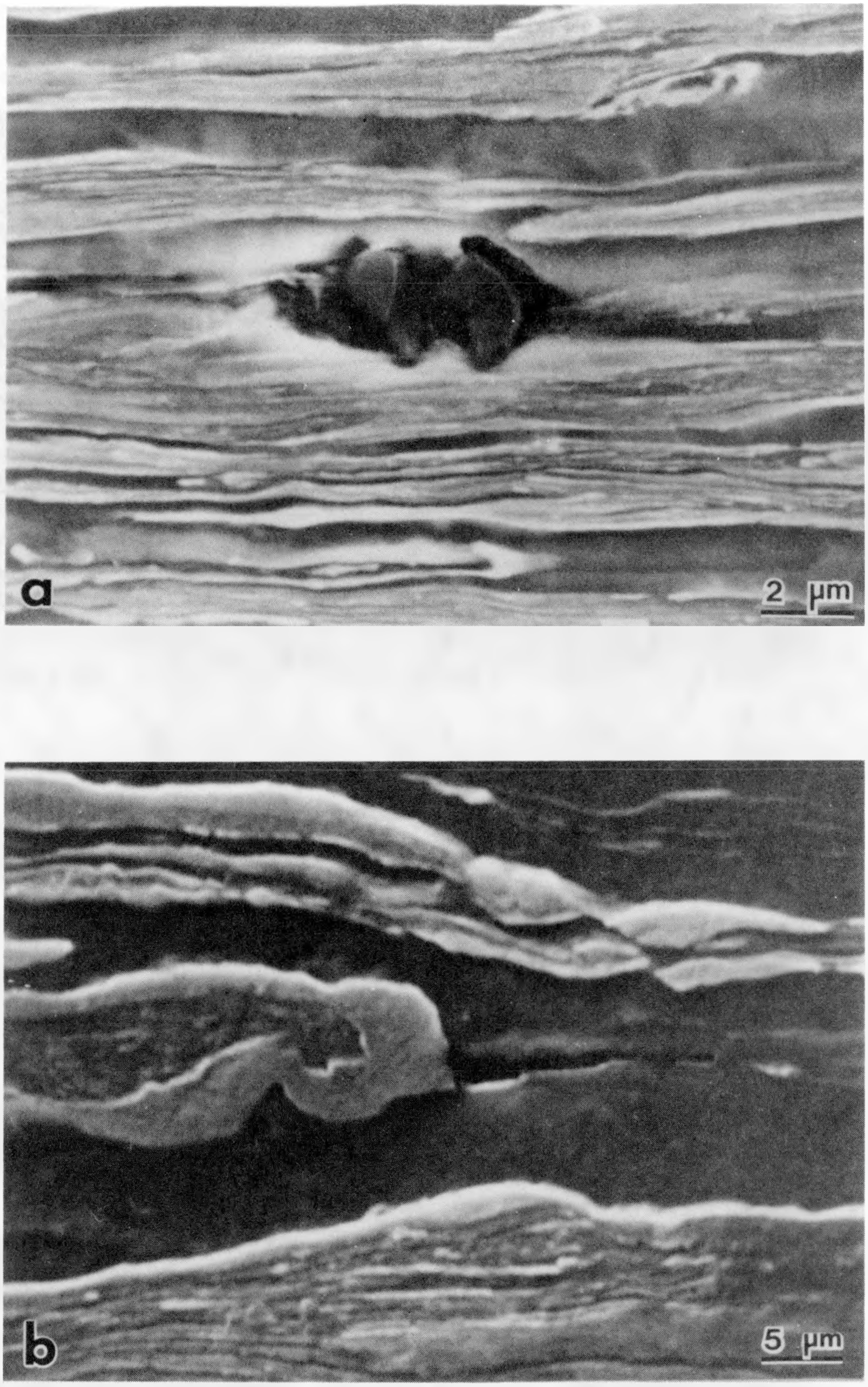

XBB 870-8534A

Figure 14. Examples of voids observed in drawn wires:
(a) void about inclusion,
(b) decohesion of ferrite/martensite interface normal to the drawing direction caused by a dead zone at the end of the martensite grain,
(c) decohesion of ferrite/martensite interface parallel to the drawing direction,
(d) shear cracking of martensite particle.

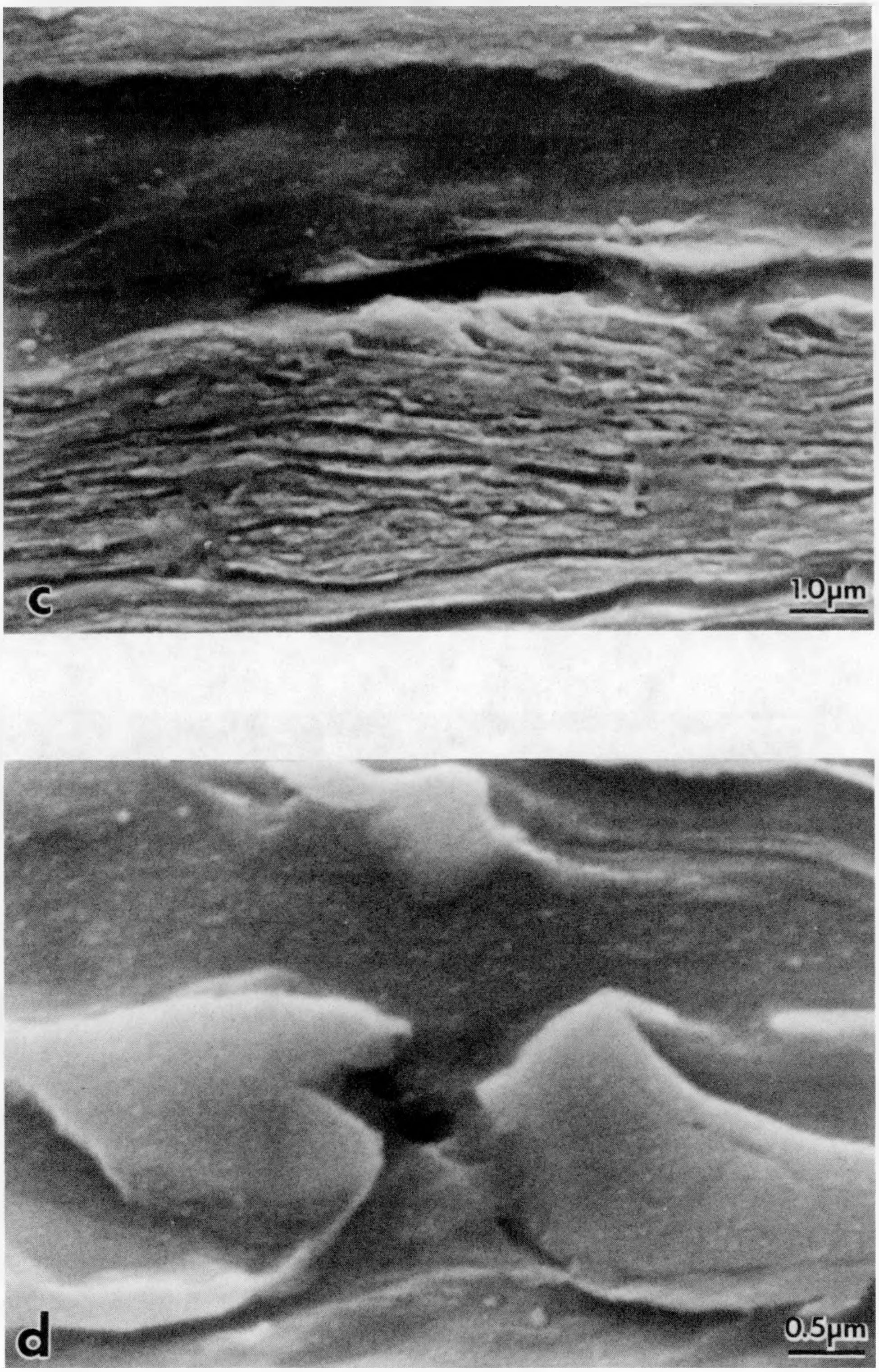

XBB 878-7020A

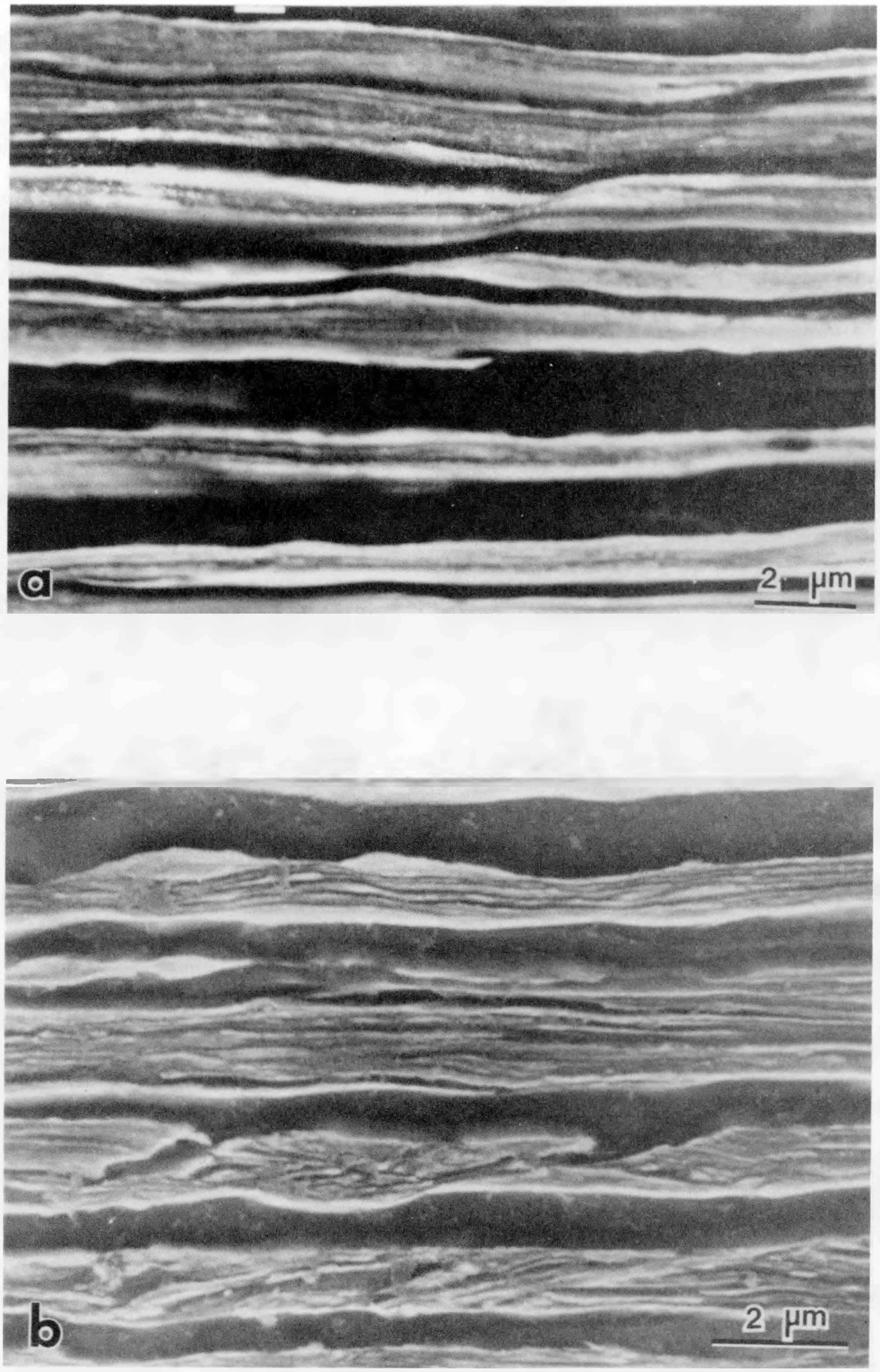

XBB 878-7014A

Figure 15. SEM micrographs of the evolution of shear failure of the martensite phase during wire drawing. (a) is from an earlier drawing pass than (b).

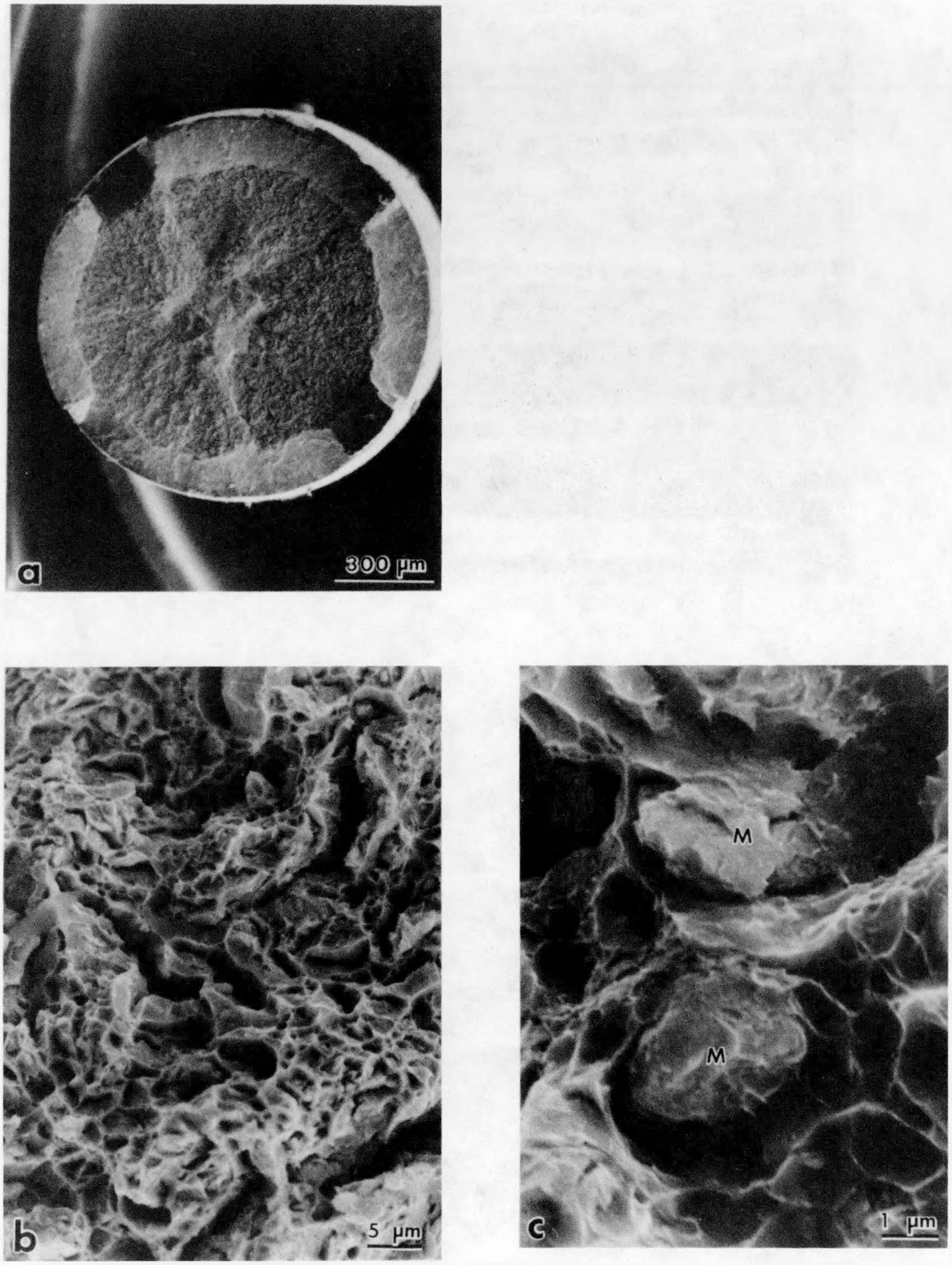

XBB 870-8491A

Figure 16. Tensile fracture surfaces of drawn wires produced by
(a), (b), (c) 0.2/IQ/30
(d), (e) 0.1/IQ/30
(f), (g) 0.1/IA/30.

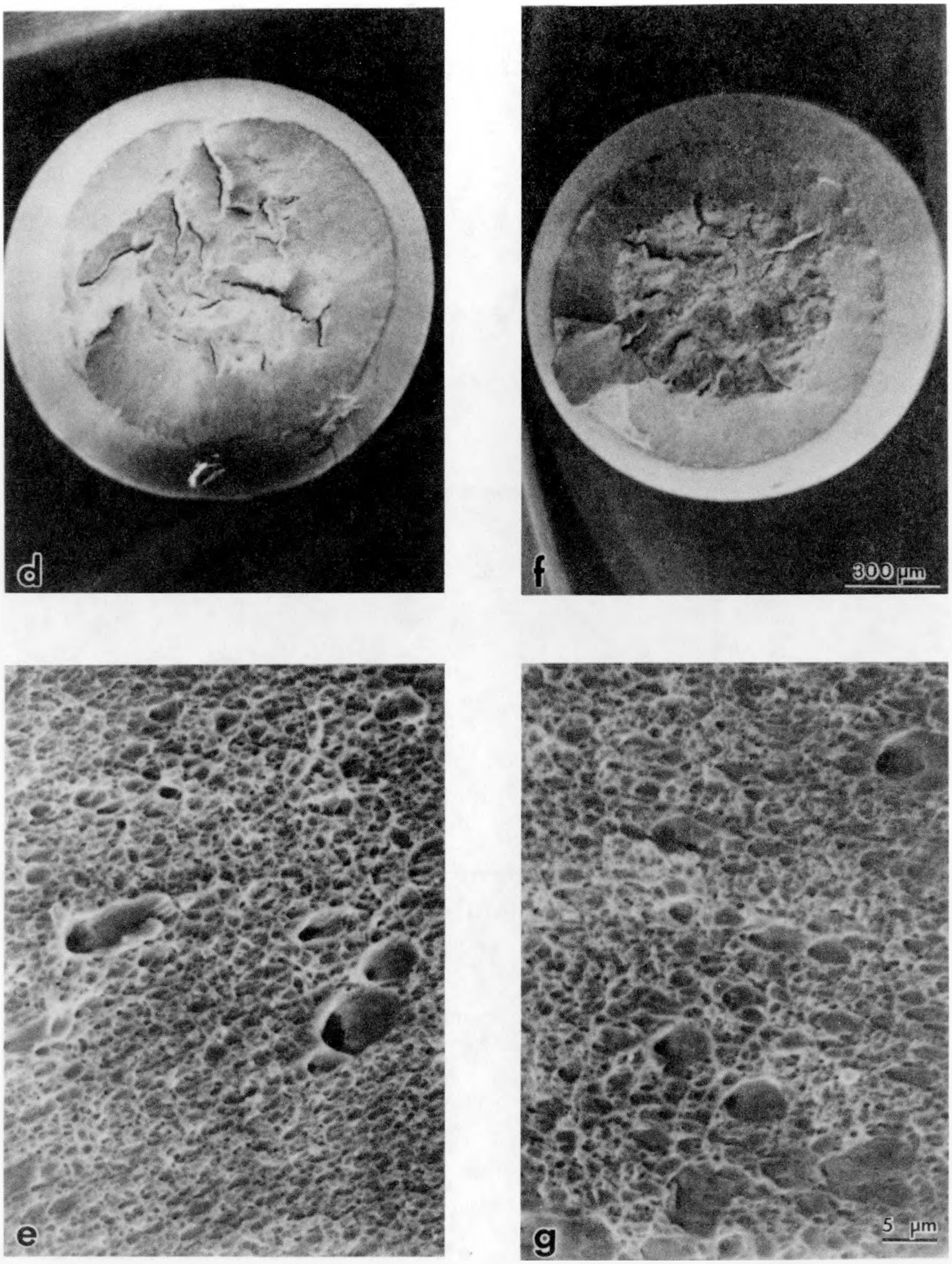

XBB 870-8530A

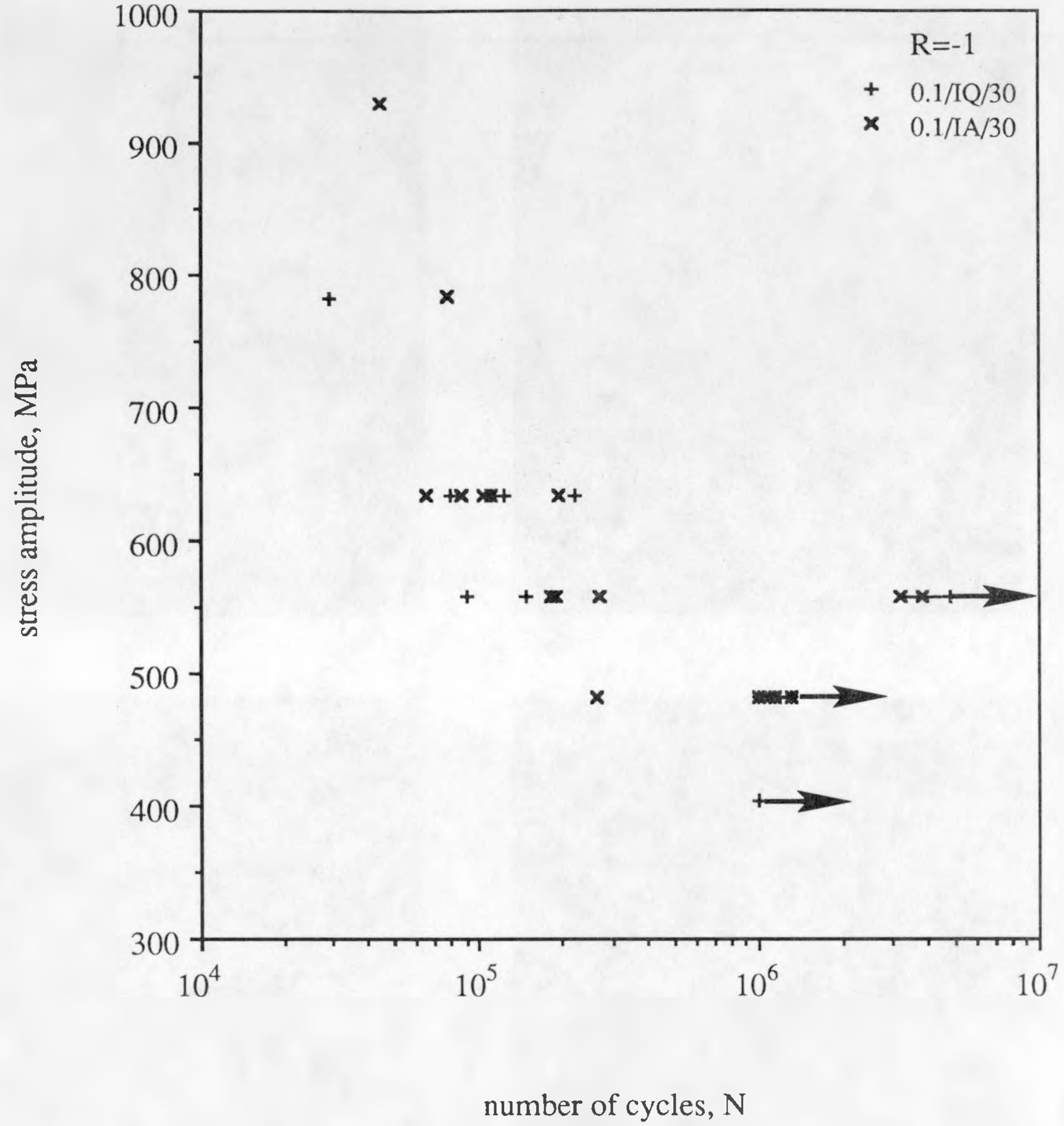

XBL 8711-4873

Figure 17. S/N curves for wires produced from 0.1/IQ/30 and 0.1/IA/30 indicates that the fatigue limit of 0.1/IA/30 may be slightly higher than 0.1/IQ/30.

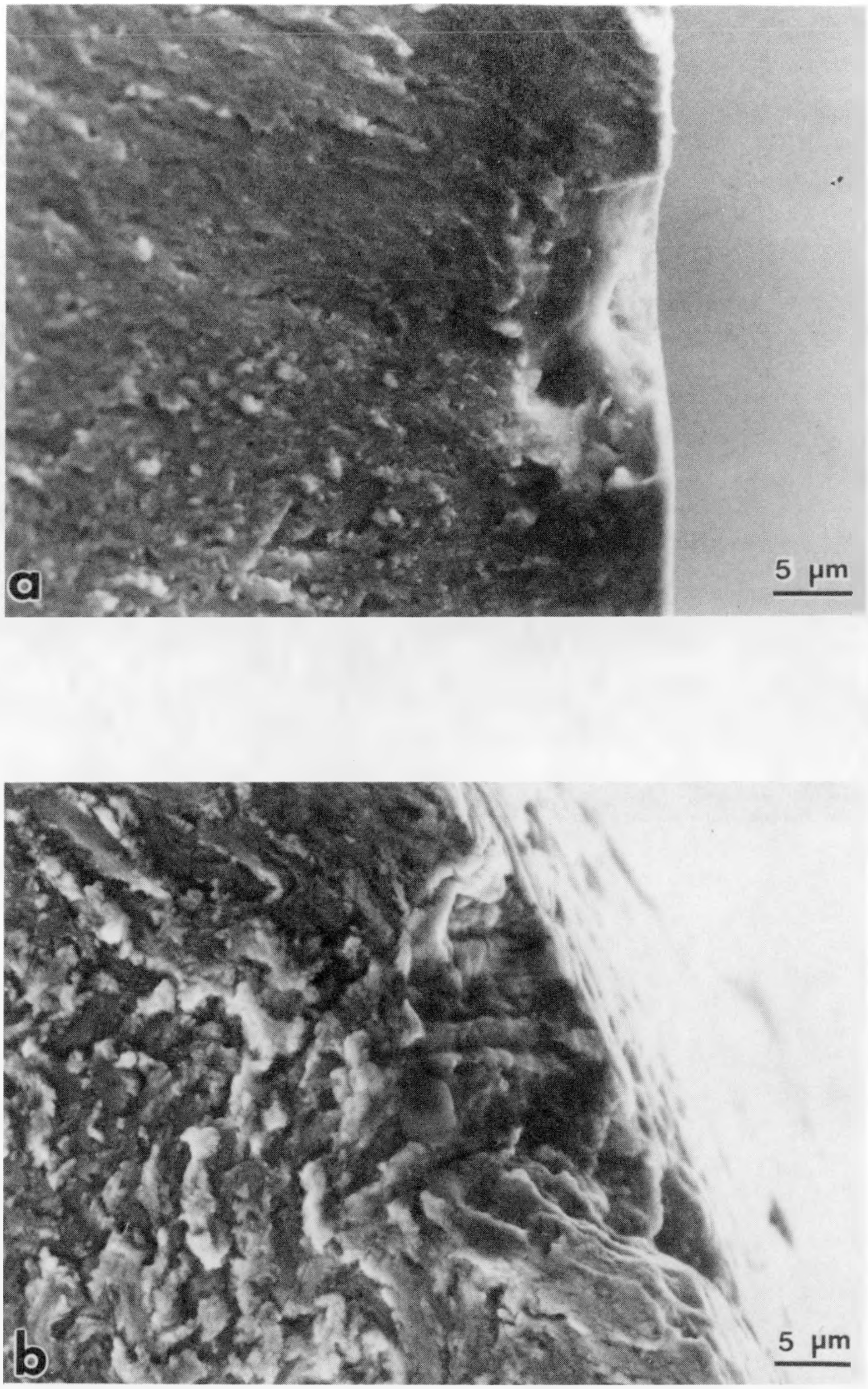

XBB 878-7018A

Figure 18. SEM micrographs of initiation sites for fatigue cracks were
(a) inclusions/holes at wire surface,
(b) decohesion of ferrite/martensite interface normal to the drawing load, or shear cracking of martensite particles,
(c) cracks in the interior of the wire which were formed during drawing.

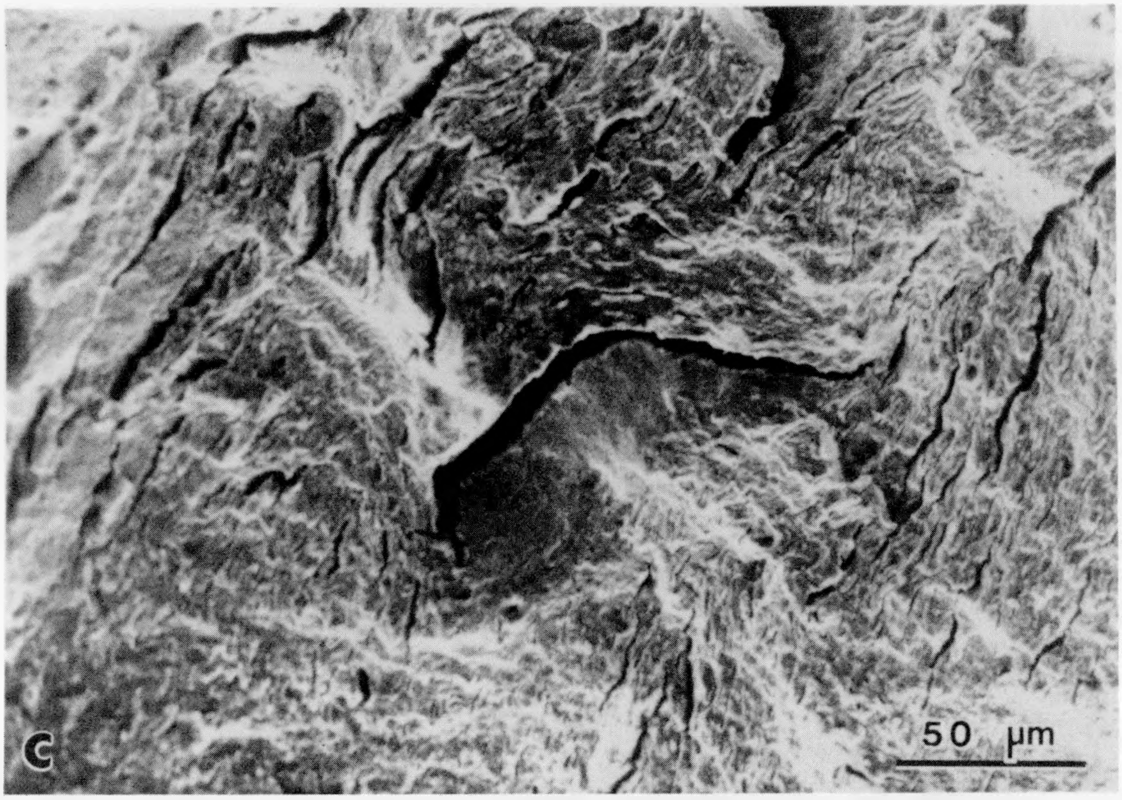

XBB 878-7011A

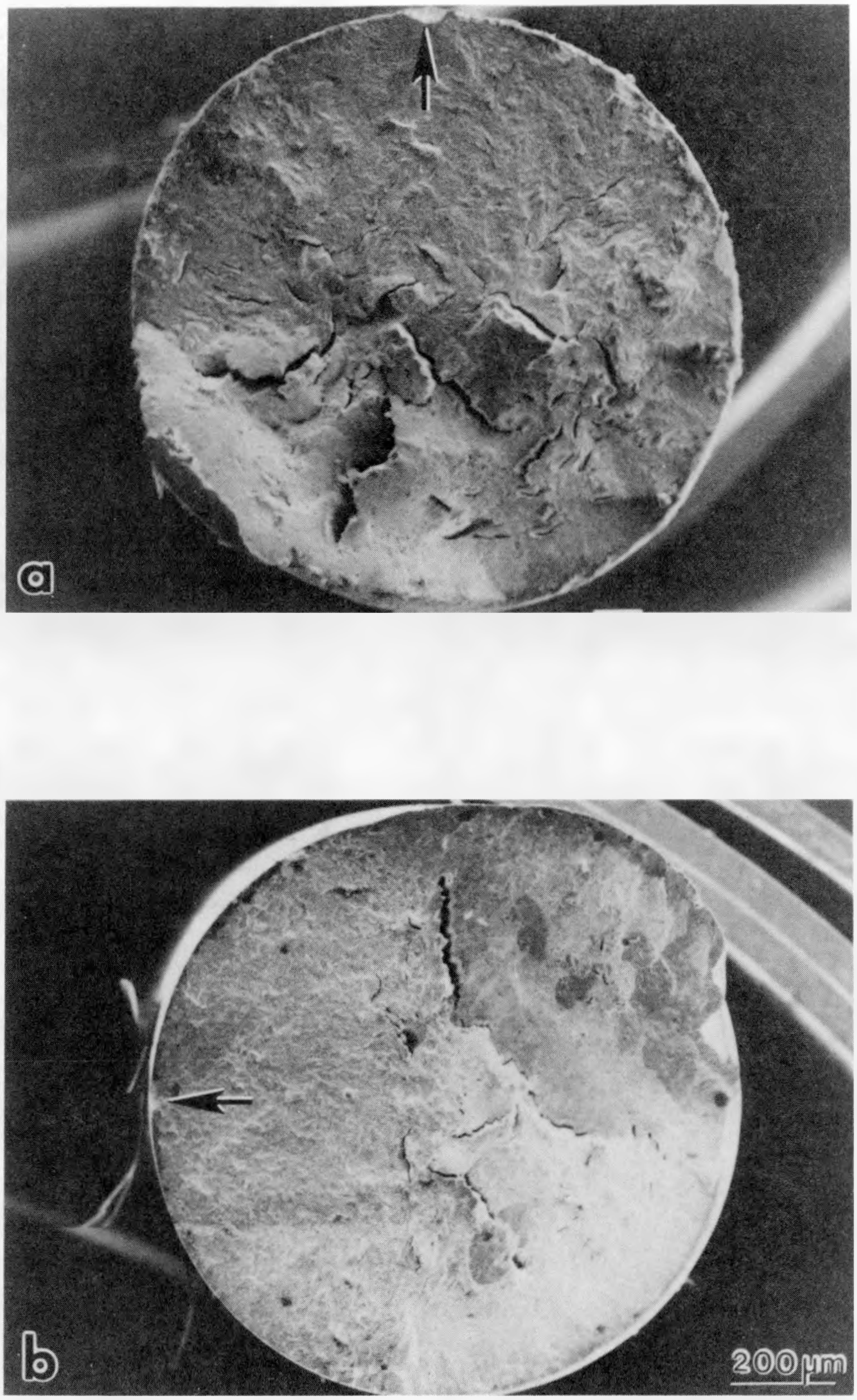

XBB 870-8489A

Figure 19. Low magnification SEM of fatigue fracture surfaces of wires drawn from (a) 0.1/IQ/30 and (b) 0.1/IA/30. Initiation sites are indicated by arrows. Fatigue zone has the typical penny-shaped outline, and the fast fracture zone contains considerable secondary cracking.

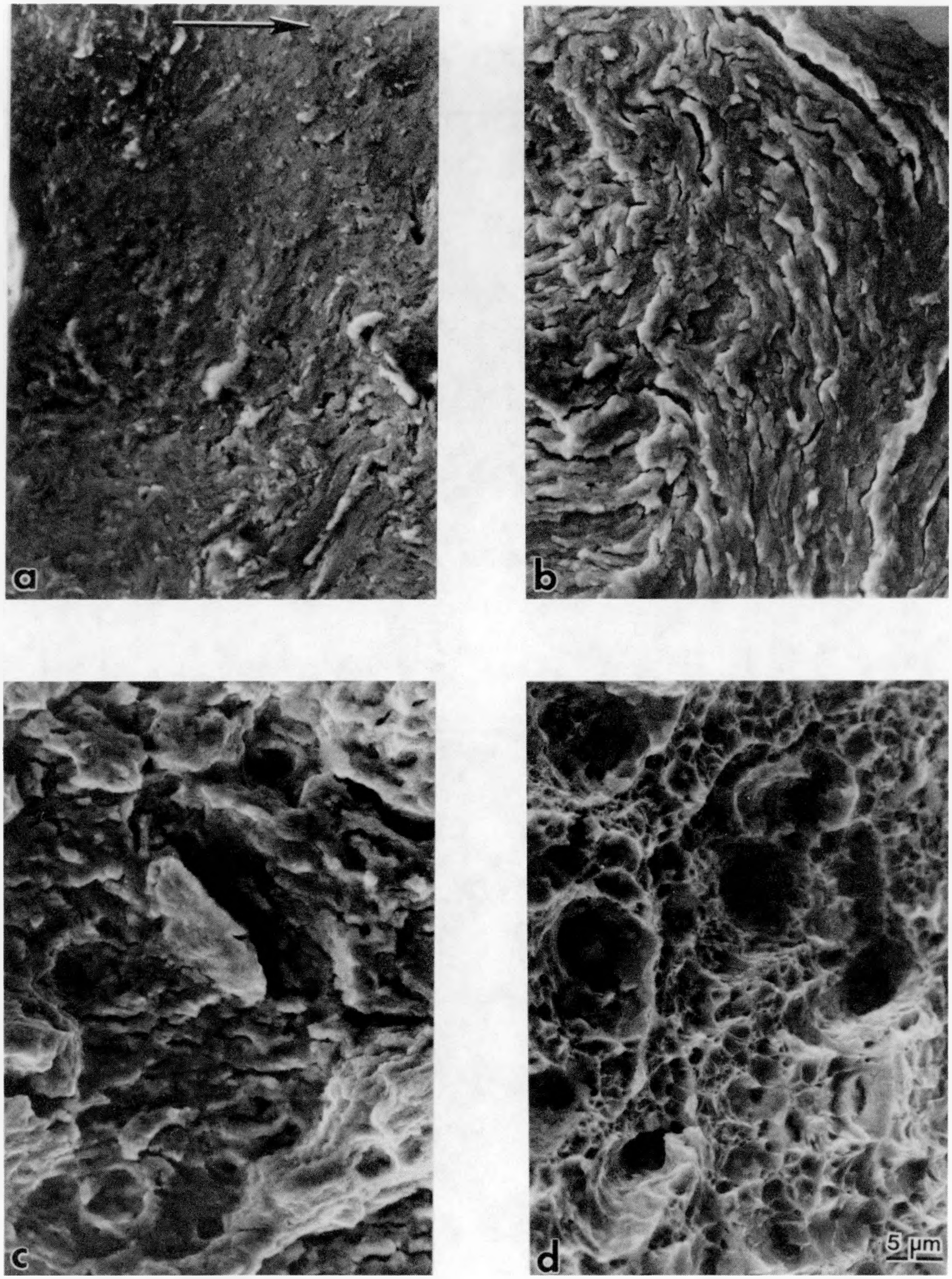

XBB 870-8899A

Figure 20. Higher magnification SEM of fatigue fracture surfaces of wires drawn from 0.1/IQ/30: (a) crack near initiation site, (b) mid-zone, (c) near end of zone, (d) ductile fast fracture.

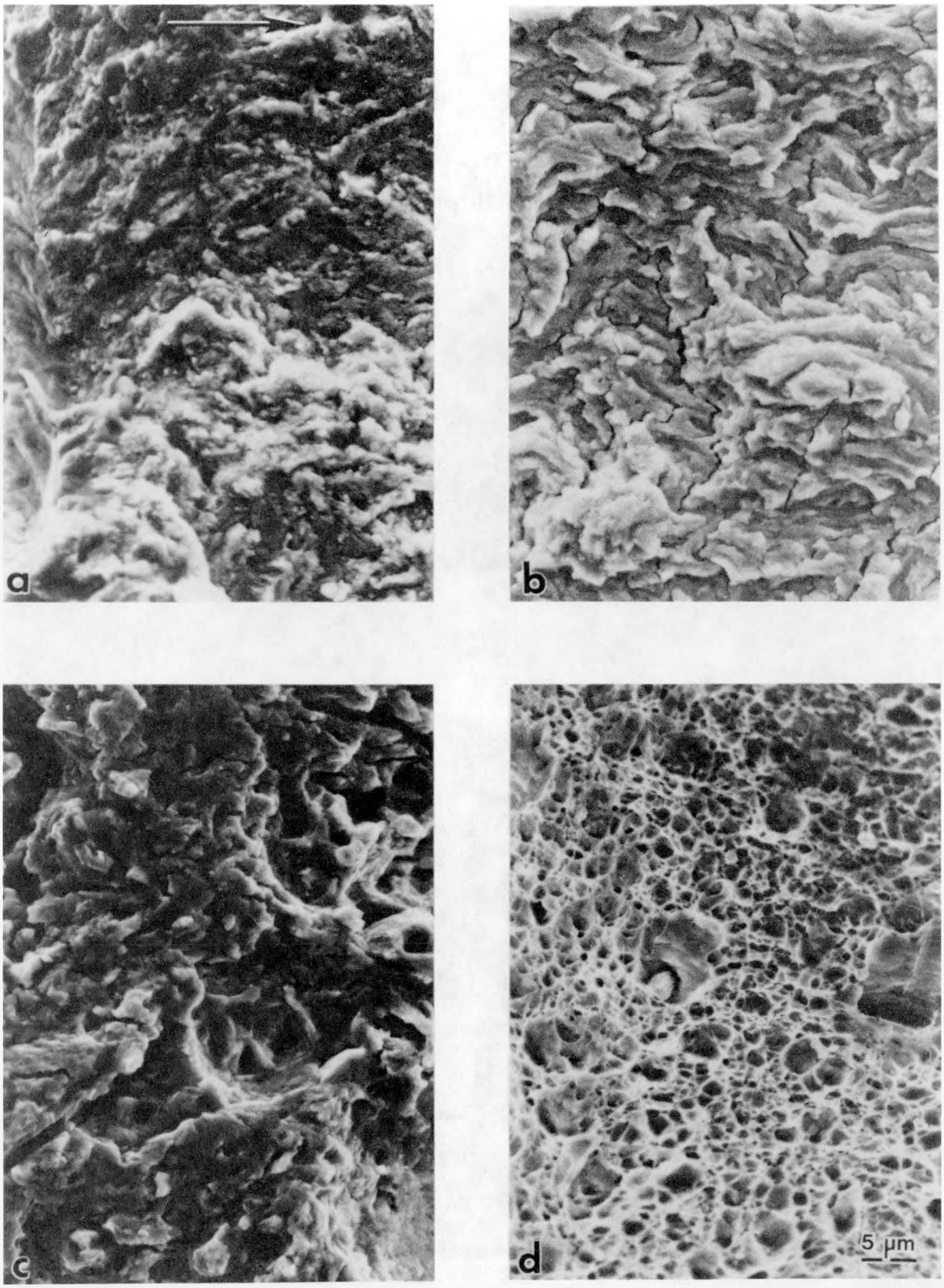

XBB 879-7362A

Figure 21. Higher magnification SEM of fatigue fracture surfaces of wire drawn from 0.1/IA/30: (a) crack near initiation site, (b) mid-zone, (c) near end of zone, (d) ductile fast fracture.

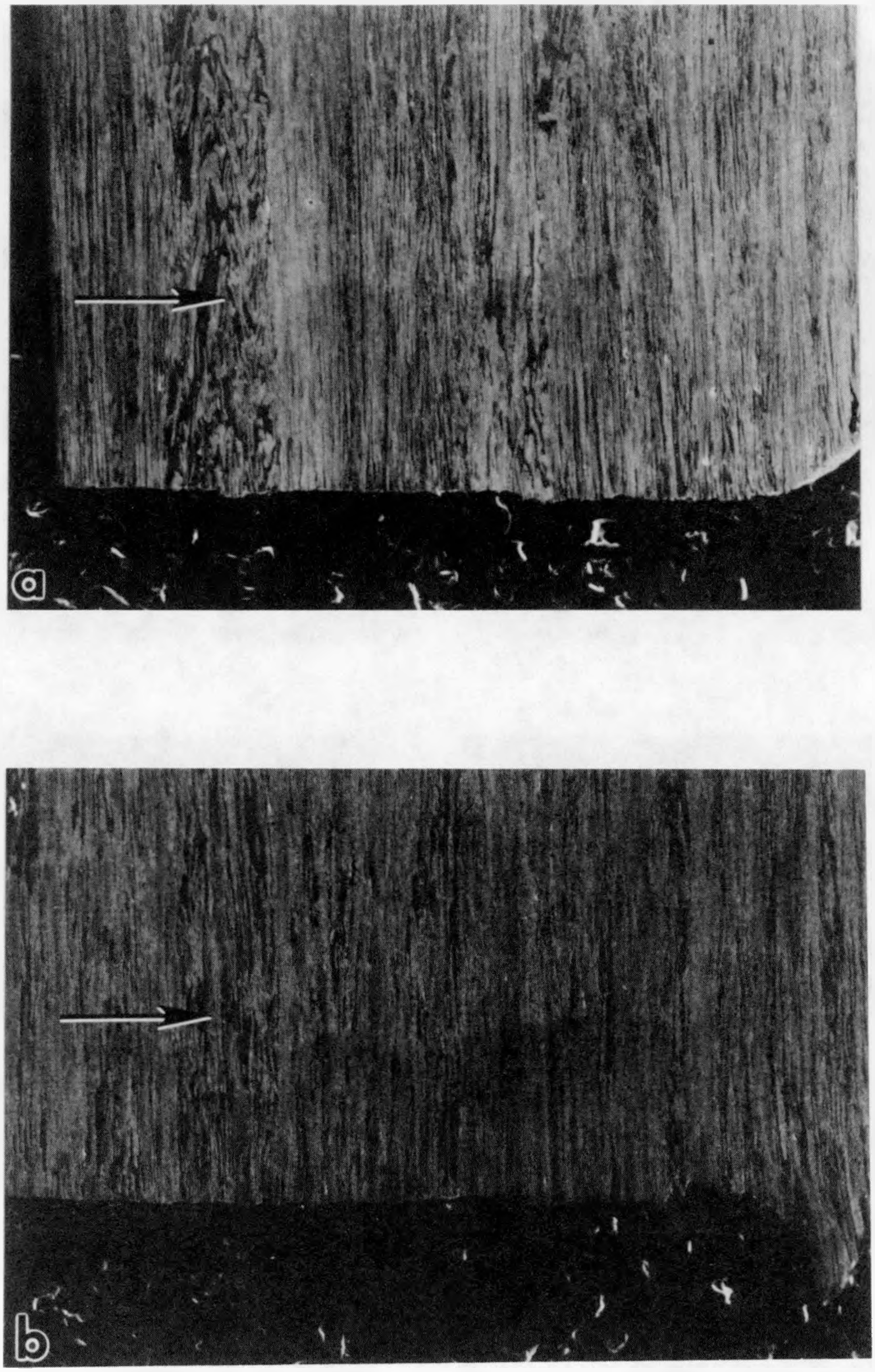

XBB 870-8893A

Figure 22. Low magnification SEM of fatigue crack profile obtained by cutting fracture surface in half longitudinally for (a) 0.1/IQ/30, and (b) 0.1/IA/30. Little deflection of the crack is seen in either IQ or IA.

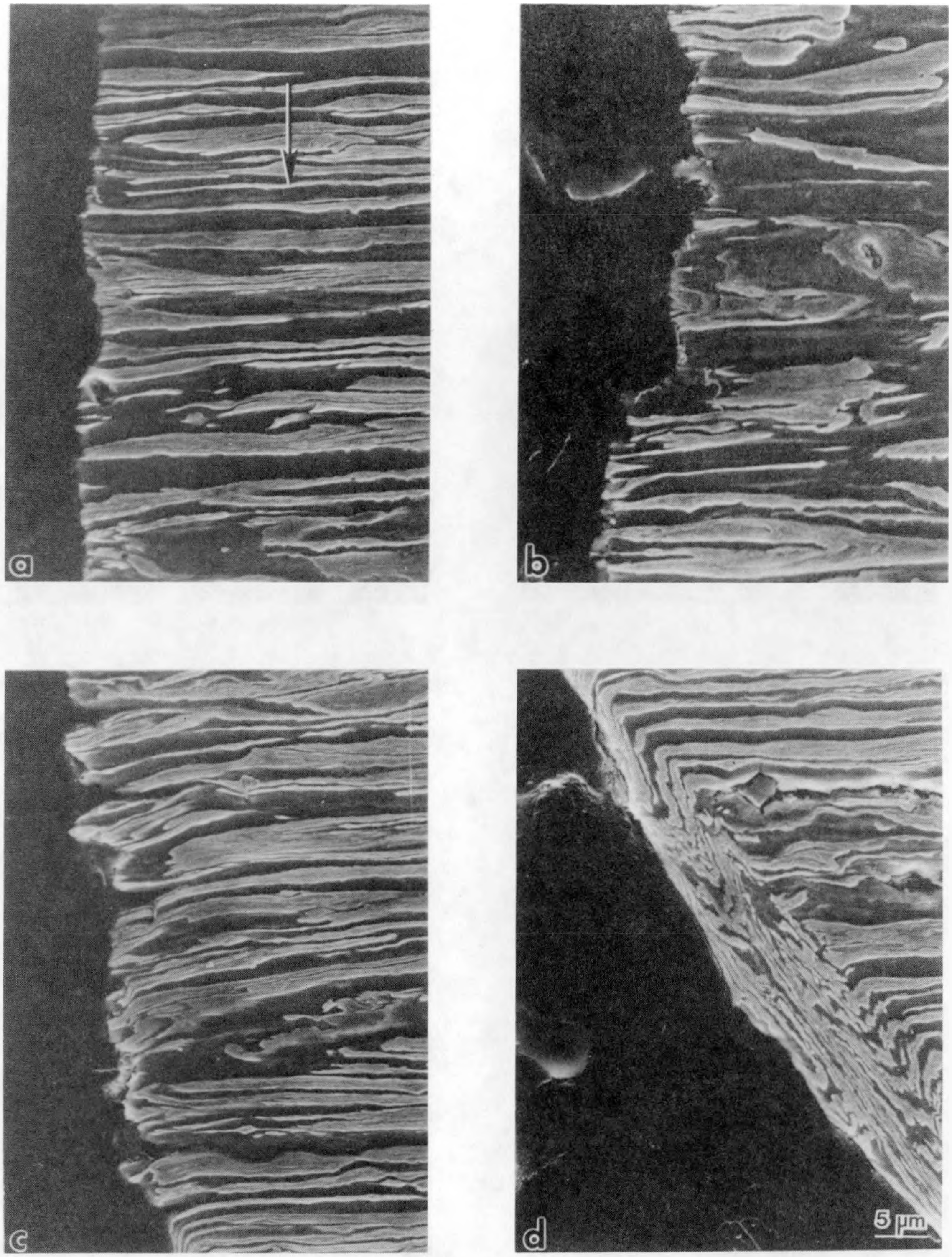

XBB 870-8889A

Figure 23. Higher magnification SEM of fatigue crack profile of 0.1/IQ/30 (crack growth direction indicated by arrow): (a) near initiation site, (b) mid-zone, (c) near end of zone, (d) fast fracture.

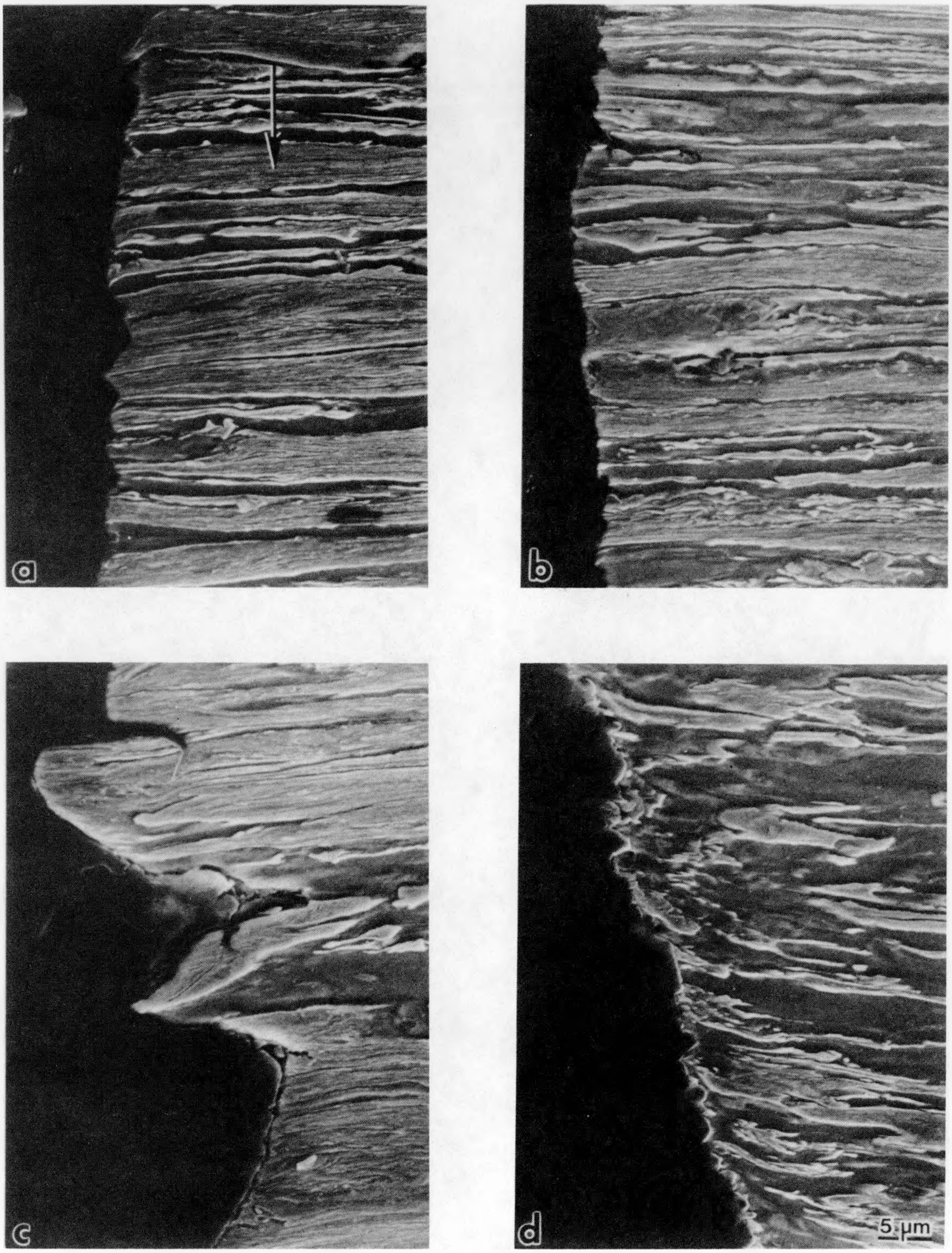

XBB 870-8499A

Figure 24. Higher magnification SEM of fatigue crack profile of 0.1/IA/30 (crack growth direction indicated by arrow): (a) near initiation site, (b) mid-zone, (c) near end of zone, (d) fast fracture.

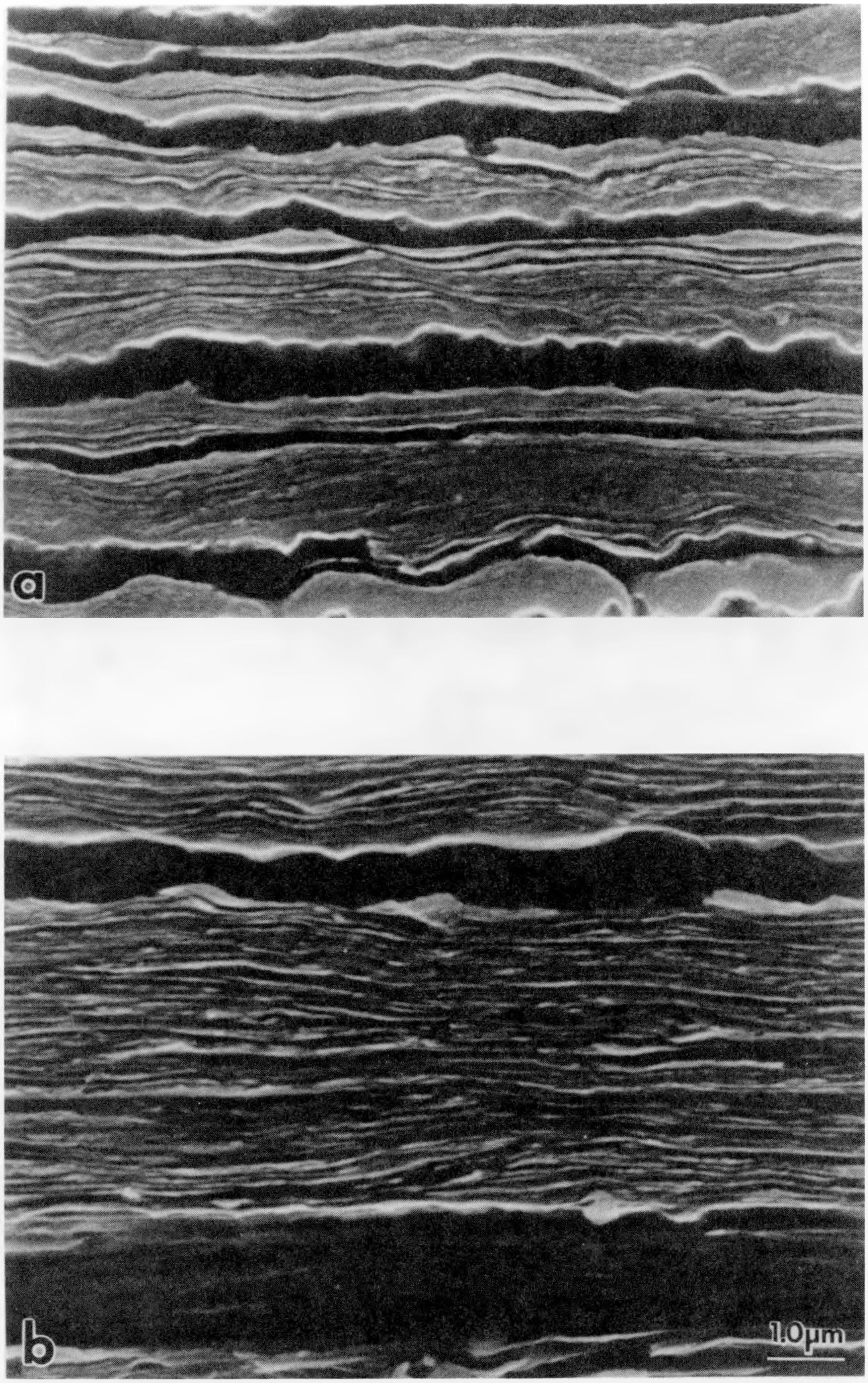

XBB 870-8895A

Figure 25. Scanning electron micrographs of martensite particles after cyclic loading for (a) 0.1/IQ/30, and (b) 0.1/IA/30. The degree of roughness at the martensite/ferrite interface is larger for IQ than IA.

Mechanism of Void Formation by Shear Cracking of Martensite

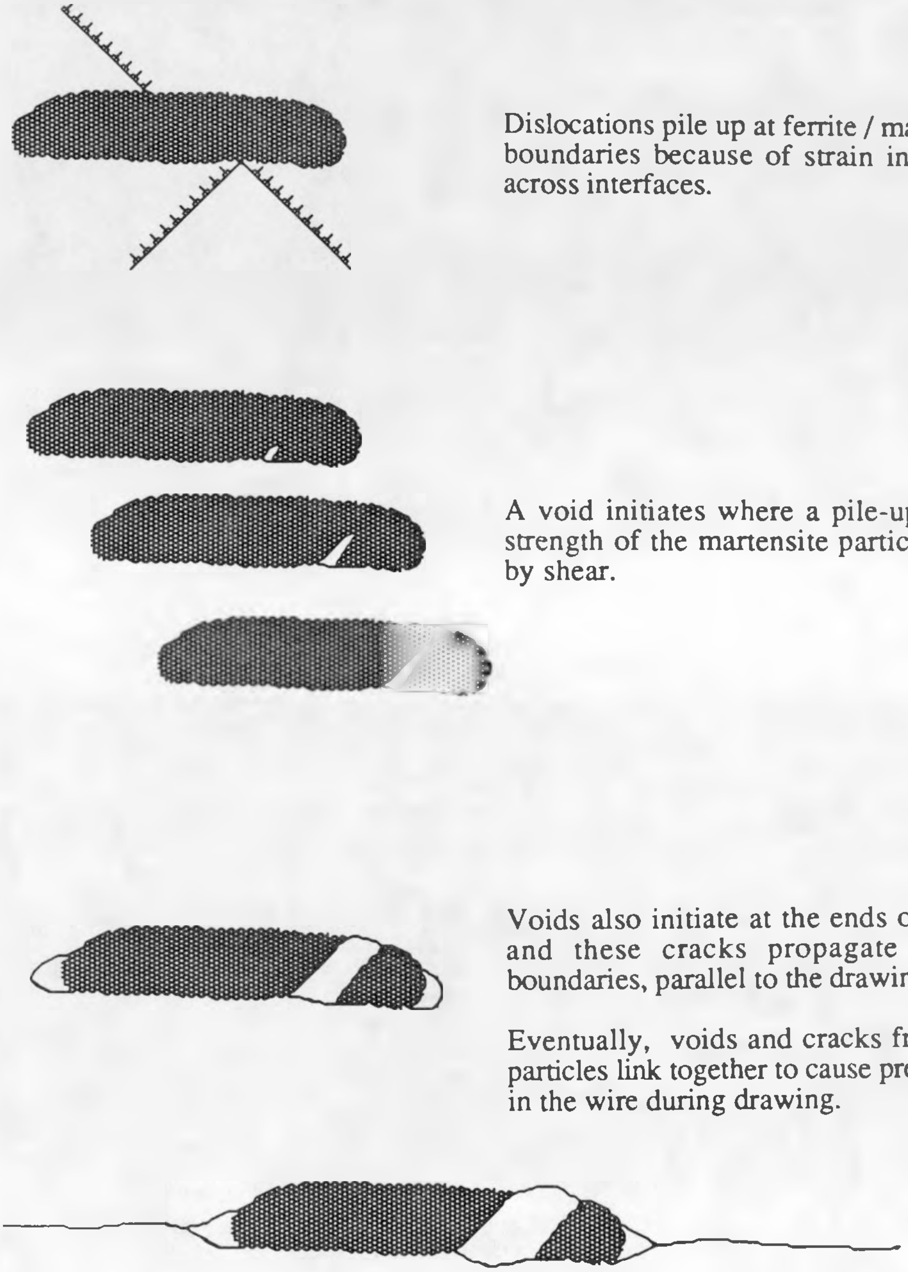

Dislocations pile up at ferrite / martensite grain boundaries because of strain incompatibility across interfaces.

A void initiates where a pile-up exceeds the strength of the martensite particle, and grows by shear.

Voids also initiate at the ends of the particle, and these cracks propagate along grain boundaries, parallel to the drawing load.

Eventually, voids and cracks from groups of particles link together to cause premature failure in the wire during drawing.

XBL 8710-4277

Figure 26. Dislocation model of shear cracking in martensite.